CrossMark

J. Fluid Mech. (2015), *vol.* 777, *pp.* 291–326. © Cambridge University Press 2015
doi:10.1017/jfm.2015.332

Unsteady flow structures around a high-drag Ahmed body

B. F. Zhang[1,2], Y. Zhou[1,†] and S. To[3]

[1]Institute for Turbulence–Noise–Vibration Interactions and Control, Shenzhen Graduate School, Harbin Institute of Technology, Shenzhen 518055, China

[2]Department of Mechanical Engineering, The Hong Kong Polytechnic University, Hung Hom, Kowloon, Hong Kong, China

[3]State Key Laboratory of Ultra-precision Machining Technology, Department of Industrial and System Engineering, The Hong Kong Polytechnic University, Hung Hom, Kowloon, Hong Kong, China

(Received 10 September 2014; revised 8 April 2015; accepted 11 June 2015; first published online 16 July 2015)

This work aims to gain a relatively thorough understanding of unsteady predominant coherent structures around an Ahmed body with a slant angle of 25°, corresponding to the high-drag regime. Extensive hot-wire, flow visualization and particle image velocimetry measurements were conducted in a wind tunnel at $Re = (0.45\text{–}2.4) \times 10^5$ around the Ahmed body. A number of distinct Strouhal numbers (St) have been found, two over the rear window, three behind the vertical base and two above the roof. The origin of every St has been identified. The two detected above the roof are ascribed to the hairpin vortices that emanate from the recirculation bubble formed near the leading edge and to the oscillation of the core of longitudinal vortices that originate from bubble pulsation, respectively. The two captured over the window originate from the hairpin vortices and the shear layers over the roof and side surface, respectively. One measured in the wake results from the structures emanating alternately from the upper and lower recirculation bubbles. The remaining two detected behind the lower edge of the base are connected to the cylindrical struts, respectively, which simulate wheels. These unsteady structures and corresponding St reconcile the widely scattered St data in the literature. The dependence on Re of these Strouhal numbers is also addressed, along with the effect of the turbulent intensity of oncoming flow on the flow structures. A conceptual model is proposed for the first time, which embraces both steady and unsteady coherent structures around the body.

Key words: separated flows, vortex interactions, wakes

1. Introduction

There has recently been renewed interest in finding new technologies to reduce aerodynamic drag and hence improve fuel consumption in the automotive industry because of the continuing high fuel costs in the past few years as well as the issue of global warming. Aerodynamic drag is responsible for more than 50 % of the

† Email address for correspondence: zhouyu@hitsz.edu.cn

https://doi.org/10.1017/jfm.2015.332 Published online by Cambridge University Press

propulsive fuel consumption of a typical car running on the highway (Hucho & Sovran 1993). With passive shaping of vehicles now approaching an optimum, it is active control that can achieve further substantial drag reduction, which calls for a thorough understanding of the flow around a ground vehicle (Joseph, Amandolese & Aider 2012). The crucial information required for the active control of drag are the unsteady flow structures around a vehicle and the corresponding Strouhal numbers St. In this paper, unless otherwise stated, the square root of the model frontal area A is used to calculate St and the Reynolds number Re.

Consider the generic Ahmed body (Ahmed, Ramm & Faltin 1984), which is perhaps the most widely studied simplified car model. Past experimental and numerical studies indicate three major components in the wake of this body: a recirculation bubble over the slanted surface or rear window, one pair of counter-rotating longitudinal or C-pillar vortices originating from the two side edges of the rear window, and a recirculation torus behind the vertical base (e.g. Krajnović 2014). Aerodynamic drag is directly linked to the interactions between these three types of coherent structures (e.g. Beaudoin & Aider 2008). The interactions depend on the slant angle (φ) of the rear window (e.g. Ahmed *et al.* 1984). Two distinct regimes have been identified, divided by $\varphi = 30^\circ$ (Hucho & Sovran 1993). At relatively small φ, the C-pillar vortices occur, which contribute to drag, on the one hand, and induce a downwash between them, on the other. This downwash enhances flow attachment on the rear window. The combined effect is drag reduction. The minimum drag occurs as φ increases to 12.5°, at which the flow appears to be two-dimensional except in the vicinity of the two C-pillar vortices (Ahmed *et al.* 1984). Once $\varphi > 15^\circ$, the pressure drag rises rapidly with increasing φ. At $\varphi = 30^\circ$, the vortices reach a maximum in strength, and so does the drag. Beyond $\varphi = 30^\circ$, the vortices burst and the drag falls despite a fully separated flow.

Flow separation and the formation of coherent structures may also take place in the front region and roof of the body (Krajnović & Davidson 2005*a*). Minguez, Pasquetti & Serre (2008) noted flow separation and then reattachment near the leading edge of the roof and the lateral sides, producing a periodically pulsating recirculation bubble. Spohn & Gillieron (2002) observed one pair of counter-rotating longitudinal vortices above the frontal roof, originating from two foci located at the two ends of the separation line, and meanwhile Kelvin–Helmholtz (KH) vortices were formed along the middle roof. However, Krajnović & Davidson (2005*a*) challenged the observation of the KH vortices based on their large-eddy simulation (LES) data and proposed that these structures along the roof were more likely three-dimensional hairpin vortices. Franck *et al.* (2009) advocated another scenario, that is, generated near the leading edge, the KH vortices evolved into hairpin vortices downstream.

The predominant vortex frequency has also received some attention, especially for the Ahmed body of $\varphi = 25^\circ$. Spohn & Gillieron (2002) found at $Re = 9.3 \times 10^3$ that the transverse KH-type vortices above the roof were characterized by frequencies exceeding 10 times the pulsation frequency of the recirculation bubble. This is supported by the numerical simulation at $Re = 8.9 \times 10^5$ of Minguez *et al.* (2008), who observed two predominant frequencies, i.e. $St = 0.174$ and 2.38, and attributed them to bubble pulsation and transverse vortices over the roof, respectively. They also noted the unsteady structure of $St = 0.314$ in the central plane above the slant, and another at $St = 0.49$ behind the base. The values are different from Boucinha, Weber & Kourta's (2011) measurements, i.e. $St = 0.18$ above the rear window and 0.36 behind the base ($Re = 2.3 \times 10^5$).

Numerous numerical simulation studies have been conducted on the flow of an Ahmed model and its control. Krajnović & Davidson (2005*b*) studied the influence of floor motion on the aerodynamics of an Ahmed model ($\varphi = 25^\circ$) at $Re = 2.3 \times 10^5$.

https://doi.org/10.1017/jfm.2015.332 Published online by Cambridge University Press

Their LES results indicated that the drag and lift were reduced by 8 % and 16 %, respectively, in the moving floor case, compared with a stationary floor. Krajnović (2014) investigated drag reduction techniques for an Ahmed model at $Re = 4.3 \times 10^5$ by deploying one array of finite-length circular cylinders upstream of the upper edge of the rear window. This control resulted in suppression of the separation region near the upper edge of the slanted surface and an increase in the strength of the C-pillar vortices near the side edges of the rear window, which led to longer separation bubbles behind the vertical base, producing a significant drag reduction by 11.6 %. The LES technique was also employed for the simulation of flow around a square-back Ahmed model of $\varphi = 0°$ (e.g. Östh *et al.* 2014). Kaiser *et al.* (2014) proposed a novel cluster-based reduced-order modelling (CROM) strategy for the simulation of the unsteady flow around an Ahmed model ($\varphi = 0°$), and their simulated unsteady wake in the model showed good agreement with experimental data. Angelis *et al.* (1996) carried out a numerical and experimental investigation on flow over a two-dimensional car model. Their calculation based on incompressible Navier–Stokes equations and a pressure correction algorithm agreed with measurements in the velocity profiles and pressure distributions over the model.

Previous investigations have improved tremendously our knowledge of the Ahmed body wake but also raised a number of issues that have yet to be addressed. The issues are important from both fundamental and applicative points of view. Firstly, the reported *St* values of unsteady flow structures around the Ahmed body of $\varphi = 25°$ are greatly scattered; the measured or calculated *St* varies between 0.18 and 0.50 over the rear window (Minguez *et al.* 2008; Thacker *et al.* 2010; Boucinha *et al.* 2011; Heft, Indinger & Adams 2011; Joseph *et al.* 2012) and between 0.36 and 0.53 behind the base (Minguez *et al.* 2008; Boucinha *et al.* 2011; Joseph *et al.* 2012). A summary of *St* reported in the literature is given in table 1. Such large scattering cannot be simply ascribed to differences in numerical schemes or experimental conditions such as *Re*, turbulence level and blockage ratio. Secondly, the well-known classical model of the flow structure is constructed based on time-averaged data (Ahmed *et al.* 1984). This model is apparently inadequate, e.g. for the purpose of active flow control. There has recently been resurgence in the active drag reduction of the Ahmed body (e.g. Brunn *et al.* 2007; Wassen & Thiele 2008, 2010; Aubrun *et al.* 2011). These efforts have achieved rather limited success due to a lack of accurate information on unsteady flow structures including *St*; the maximum drag reduction reported is only approximately 14 % (Aubrun *et al.* 2011), substantially below the target set by the automotive industry (e.g. Bruneau *et al.* 2011). There have been scattered reports on unsteady flow structures over the roof, side surface, rear window and base of the Ahmed body. However, the connection between the structures over the different regions of the body has never been made clear and the full picture of the unsteady flow around the body remains elusive. Thirdly, up to now there has been no consensus on the dependence of *St* on *Re*. For instance, Thacker *et al.* (2010) reported a slight increase in *St* from 0.22 to 0.25 over the rear window with *Re* increasing from 4.5×10^5 to 9.0×10^5 based on hot-wire measurements. But Joseph *et al.* (2012) measured using the hot-wire technique a significant rise in *St* from 0.33 to 0.50 over the rear window with a change in *Re* from 4.5×10^5 to 6.8×10^5. Finally, numerous investigations to simulate the flow numerically call for a more complete experimental database for the validation of computational fluid dynamics (CFD) codes.

This work aims to address the above-mentioned unresolved issues through a relatively thorough experimental investigation on the wake of the Ahmed model of $\varphi = 25°$, and to provide experimental data for the validation of the CFD codes.

https://doi.org/10.1017/jfm.2015.332 Published online by Cambridge University Press

https://doi.org/10.1017/jfm.2015.332 Published online by Cambridge University Press

Researchers	Investigation techniques	*Re*	Locations	*St*
Spohn & Gillieron (2002)	Flow visualization	9.3×10^3	In the symmetry plane above the roof	0.22, 2.64
Minguez *et al.* (2008)	LES simulation	8.9×10^5	In the symmetry plane above the roof	0.20, 2.38
			In the symmetry plane over the slanted surface	0.31
			In the symmetry plane behind the base	0.49
Thacker *et al.* (2010)	Hot-wire measurement	$(4.6–9.2) \times 10^5$	In the symmetry plane over the slanted surface	0.22–0.25
Boucinha *et al.* (2011)	Hot-wire measurement	2.3×10^5	In the symmetry plane over the slanted surface	0.18
			In the symmetry plane behind the base	0.36
Heft *et al.* (2011)	Wall pressure measurement	8.5×10^5	In the symmetry plane on the slanted surface	0.18
			Near the side edge of the slanted surface	0.30
Joseph *et al.* (2012)	Hot-wire measurement	$(4.5–6.8) \times 10^5$	In the symmetry plane over the slanted surface	0.33–0.50
			In the symmetry plane behind the base	0.51–0.53
Thacker *et al.* (2013)	Hot-wire and wall pressure measurements	7.1×10^5	In the symmetry plane over the slanted surface	0.23

TABLE 1. Summary of the Strouhal numbers *St* around an Ahmed model ($\varphi = 25°$) reported in the literature.

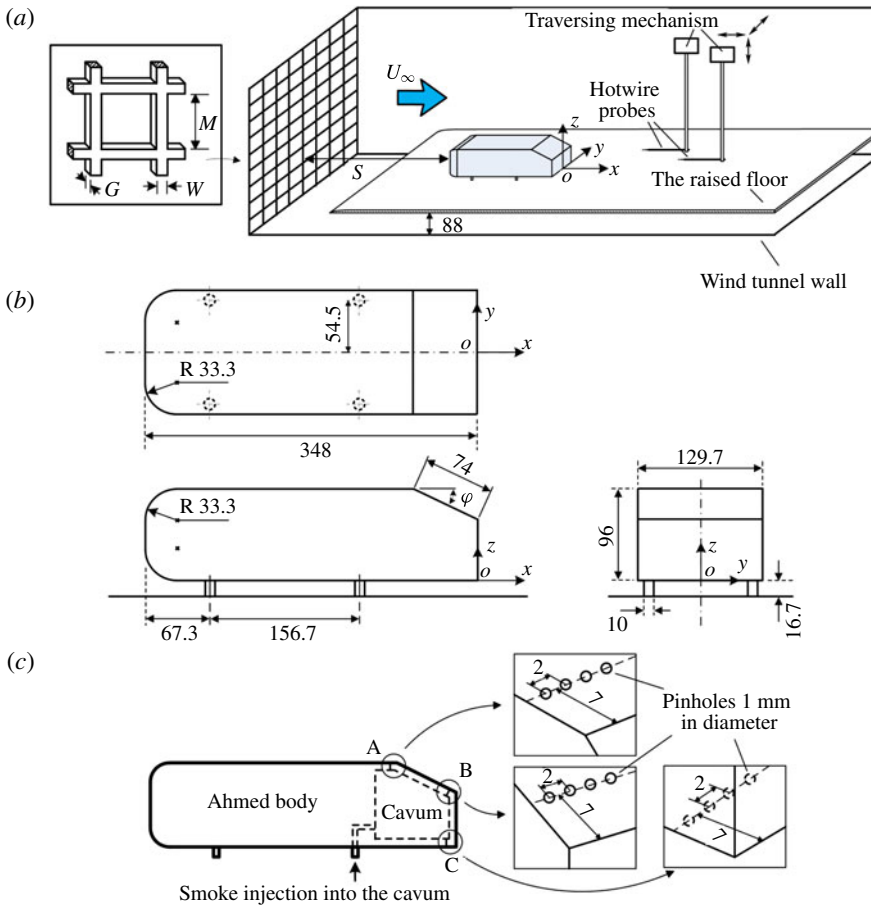


FIGURE 1. (Colour online) (*a*) Schematic of experimental arrangement. (*b*) Dimensions of a one-third scale Ahmed body. (*c*) Smoke release points in flow visualization experiments. The length unit is millimetre and angle is in degree.

Experimental details are given in § 2. The captured unsteady flow structures and their corresponding *St* values are presented in § 3. The origins of the structures are unveiled in § 4. The Reynolds number effect on *St* is examined in § 5. The effect of the turbulent intensity of the oncoming flow on the unsteady structures is discussed in § 6. A conceptual model of the flow structure around the Ahmed body is proposed in § 7. This work is concluded in § 8.

2. Experimental details

Experiments were carried out in a closed-circuit wind tunnel with a 2.4 m long square test section (0.6 m × 0.6 m). The flow non-uniformity is 0.1 % and the longitudinal turbulence intensity T_u is 0.3 % in the test section. See Huang, Zhou & Zhou (2006) for more details of the tunnel. The experimental set-up is schematically shown in figure 1(*a*). A flat plate of 2.2 m × 0.59 m × 0.015 m with a clipper-built leading edge is installed horizontally, 0.088 m above the floor of the test section, as a raised floor to control the boundary layer thickness. Its leading edge is 0.3 m downstream of the exit plane of the tunnel contraction.

https://doi.org/10.1017/jfm.2015.332 Published online by Cambridge University Press

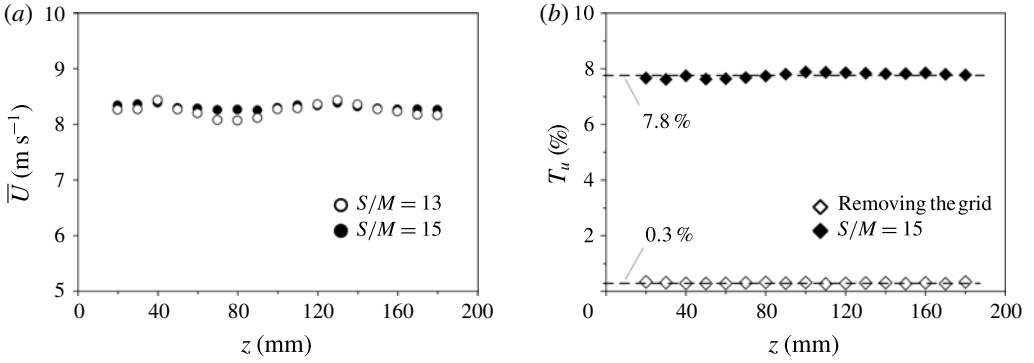


FIGURE 2. (*a*) The distribution of $\overline{U}$ at $S/M = 13$ and 15. (*b*) The distribution of T_u of removing the grid and at $S/M = 15$.

The vehicle model was a one-third scale Ahmed body (Ahmed *et al.* 1984). The angle φ of the slanted surface was 25°, at which the wake is characterized by one pair of strong counter-rotating streamwise vortices. This configuration has been deployed to represent the high-drag regime and rather extensively investigated (e.g. Minguez *et al.* 2008). The test model was placed on the raised floor, resulting in a blockage ratio of approximately 4.1 %. Its front end was 0.3 m, where the boundary layer thickness was approximately 4 mm at a free-stream velocity (U_∞) of 8.33 m s^{-1}, downstream of the floor leading edge. Figure 1(*b*) shows the definition of the right-handed Cartesian coordinate system (x, y, z), with the origin o at the midpoint of the lower edge of the model vertical base. The model has an overall length of $L = 0.348$ m, a width of $W = 0.13$ m and a height of $H = 0.096$ m, supported by four hollow cylindrical struts of 16.67 mm length and 10 mm diameter. In this paper, a superscript asterisk denotes normalization by $\sqrt{A}$ ($= 0.112$ m), e.g. $x^* = x/\sqrt{A}$, $y^* = y/\sqrt{A}$ and $z^* = z/\sqrt{A}$.

The higher T_u was obtained by deploying a grid upstream of the model. The characteristic dimensions of the grid are $M = 40$ mm, $W = 10$ mm and $G = 10$ mm, with a porosity of 64 % (figure 1*a*). The grid was installed at the end of the tunnel contraction section, generating closely uniform and isotropic turbulence (Wang *et al.* 2014). A calibrated hot-wire probe was used to measure the instantaneous streamwise velocity U and T_u. A variation in T_u was achieved by changing the distance S from the grid to the model frontal face. The choice of S is based on two considerations, i.e. a suitable T_u and the uniformity of $\overline{U}$, where U was measured at a number of points along the z direction and the overbar denotes time averaging. As shown in figure 2(*a*), there is a discernible variation in $\overline{U}$ across the flow at $S = 13M$ but not so at $S = 15M$. Two turbulent intensity levels, i.e. $T_u = 7.8$ % and 0.3 %, of the flow are investigated, obtained in the presence ($S = 15M$) and absence of the turbulence generator (grid), respectively (figure 2*b*).

Single hot wires fixed on a computer-controlled Dantec traverse system were used to measure streamwise fluctuating velocity u to detect the predominant frequencies in the flow (figure 1*a*). The sensing element was a tungsten wire of 5 μm diameter and approximately 1 mm in length. The wire was operated on a constant-temperature circuit (Dantec Streamline) at an overheat ratio of 1.8. The signal from the wire was offset, amplified and low-pass-filtered at a cut-off frequency of 1.0 kHz, and digitized at a sampling frequency f_s of 3.0 kHz using a 16-bit analogue-to-digital converter (NI PCI-6143). The sampling duration was 1 min, producing a total of 1.8×10^5 data

https://doi.org/10.1017/jfm.2015.332 Published online by Cambridge University Press

for each record. At least three records were collected for each measurement location. Presumably, flow is symmetric with respect to the plane $y^* = 0$. As such, the hot-wire measurements were performed only on the side of $y^* = 0$ and covered the regions of $x^* = -2.33$ to -0.74, $y^* = 0$ to 0.58 and $z^* = 0.91$ to 1.09 above the roof, and $x^* = -2.33$ to -0.74, $y^* = 0.63$ to 0.81 and $z^* = 0$ to 0.86 over the side surface, with increments of $\Delta x^* = 0.53$ and $\Delta y^* = \Delta z^* = 0.036$. The measurement ranges were $x^* = -0.51$ to 0, $y^* = 0$ to 0.58 and $z^* = 0.68$ to 0.86 over the rear window, with increments of $\Delta x^* = 0.17$ and $\Delta y^* = \Delta z^* = 0.036$, and $x^* = 0.20$ to 2.20, $y^* = 0$ to 0.72 and $z^* = 0$ to 0.81 behind the base, with increments of $\Delta x^* = 0.20$ and $\Delta y^* = \Delta z^* = 0.09$. The total number of measurement points amount to more than 2200. The fast Fourier transform (FFT) algorithm was employed to calculate the power spectral density function, E_u, of u or the spectral phase between two simultaneously captured hot-wire signals. The FFT window size N_w was 4096. The frequency resolution Δf in the spectral analysis depends on the sampling frequency and the FFT window size ($\Delta f = f_s/N_W$) and is estimated to be 0.73 Hz, following Zhou *et al.* (2012). Measurements were conducted at $U_\infty = 6$–32 m s^{-1}, corresponding to $Re = (0.45$–$2.4) \times 10^5$. The wind speed was measured using a Pitot static tube connected to an electronic micro-manometer (Furness Control Ltd, FC510).

A Dantec standard particle image velocimetry (PIV) system was used to measure flow around the Ahmed model at $Re = 0.62 \times 10^5$. The flow was seeded by smoke generated from paraffin oil, with particles approximately 1 μm in diameter. Flow illumination was provided by two New Wave standard pulsed laser sources of 532 nm wavelength, each with a maximum energy output of 120 mJ per pulse. Each laser pulse lasted for 0.01 μs. Particle images were taken using a charge-coupled device (CCD) camera (HiSense type 4M, double frames, 2048 pixel × 2048 pixel). Synchronization between image taking and flow illumination was provided by the Dantec FlowMap processor (System HUB). PIV measurements were performed in the (x, z) plane at $y^* = 0$ (symmetry plane), and the (y, z) plane at $x^* = 0.20$. The PIV images covered an area of $2.1\sqrt{A} \times 2.1\sqrt{A}$, i.e. $x^* = -0.6$ to 1.5 and $z^* = -0.3$ to 1.8, and $y^* = -1.05$ to 1.05 and $z^* = -0.3$ to 1.8 for the (x, z) and (y, z) planes, respectively. The image magnifications in both directions of the plane were identical, ranging from 103 to 113 μm pixel^{-1}. The interval between two successive pulses was 50 μs for measurements in the (x, z) plane, during which fluid particles may travel a distance of 0.42 mm at $U_\infty = 8.33$ m s^{-1}. Following Huang *et al.* (2006), the laser sheet was made thicker for measurements in the (y, z) plane, i.e. 3 mm (cf. 1.0–1.5 mm in the (x, z) plane) in order to capture the maximum number of seeding particles during each pulse. In processing PIV images, 32×32 interrogation areas were used with a 50 % overlap in each direction, producing 127×127 in-plane velocity vectors and the same number of vorticity data ω_x^* or ω_y^*. A total of 1200 PIV images were captured in each plane.

Laser-induced fluorescence (LIF) flow visualization was conducted using the same PIV system. Three rows of pinholes, each consisting of 64 circular orifices, 1 mm in diameter and equally separated by 1 mm, were made along parallel lines 7 mm upstream of the upper edge of the rear window, the upper and the lower base edges, respectively (figure 1*c*). Smoke generated by an Atomizer Aerosol Generator (TSI 3079) using DEHS oil was pumped through one hollow strut into the cavity in the rear part of the model and released into the flow through the pinholes. Flow images were taken in the (x, z) planes at $y^* = 0$ and 0.36 over the rear window and at $y^* = 0$ and 0.45 behind the base, and in the (y, z) plane at $x^* = 1.4$ in the wake.

https://doi.org/10.1017/jfm.2015.332 Published online by Cambridge University Press

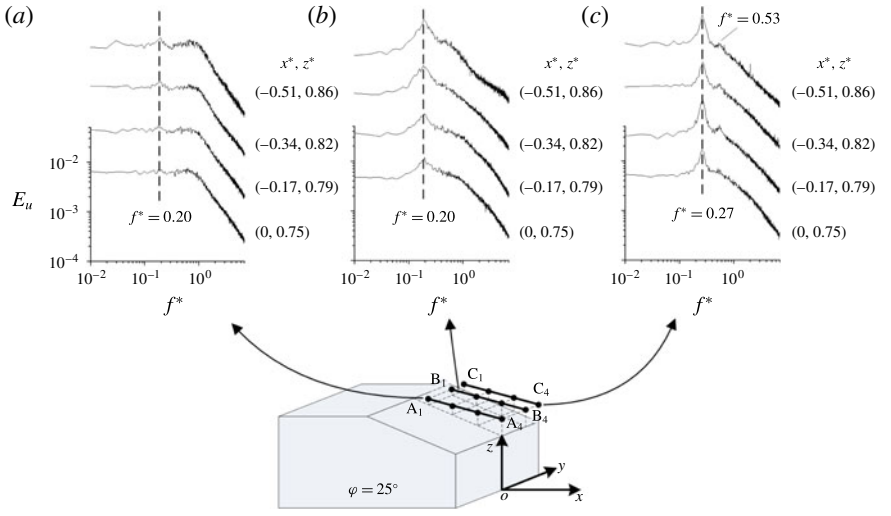


FIGURE 3. Power spectral density function E_u of the hot-wire signal measured along A_1–A_4 ($y^* = 0$), B_1–B_4 ($y^* = 0.36$), C_1–C_4 ($y^* = 0.58$), respectively, over the slant surface.

3. Flow structures and predominant frequencies in the wake

The wake is highly complicated. In this section we will present and discuss measurement results separately for the region over the rear window and that behind the vertical base. For clarity, we will first examine the data at one Reynolds number, i.e. $Re = 0.62 \times 10^5$, in this section and also in § 4 and then move on to discussing the effect of Re in § 5.

3.1. *Spanwise unsteady flow structure over the rear window*

Let us examine the downstream evolution of E_u along A_1–A_4 in the symmetry plane ($y^* = 0$). A peak in E_u (figure 3*a*) at $f^* = St_r = 0.20$, where subscript r denotes the region above the rear window, is evident at A_1 and A_2 near the upper edge of the rear window. This peak remains discernible further downstream at A_3 but vanishes at A_4. Minguez *et al.* (2008) observed numerically at $\varphi = 25°$ and $Re = 8.9 \times 10^5$ a predominant peak at $St_r = 0.314$ in E_u at a position near A_1 in the symmetry plane over the rear window. Their St_r is significantly higher than our measurement (0.20). They observed flow separation at the upper edge of the rear window and then reattachment on the slanted surface, which formed a recirculation bubble. The KH instability occurs in the shear layer above the recirculation bubble, which leads to the rollup of spanwise vortices. They ascribed this St_r to thus formed vortices over the rear window. Thacker *et al.* (2010) reported a peak in E_u at essentially the same St_r (≈ 0.20) based on hot-wire measurements at $Re = (4.5\text{–}9.0) \times 10^5$ at a position near A_1. They suggested that this unsteadiness was mainly due to the flapping recirculation bubble on the slant. A different view will be proposed presently based on our flow visualization data.

A peak occurs at $f^* = St_r = 0.20$ in E_u for all the measurement locations along B_1–B_4 in the off-symmetry plane of $y^* = 0.36$ (figure 3*b*) and is much more pronounced than that measured along A_1–A_4. On the other hand, a relatively sharp peak occurs at $f^* = St_r = 0.27$ near the side edge of the rear window (C_1–C_4,

https://doi.org/10.1017/jfm.2015.332 Published online by Cambridge University Press

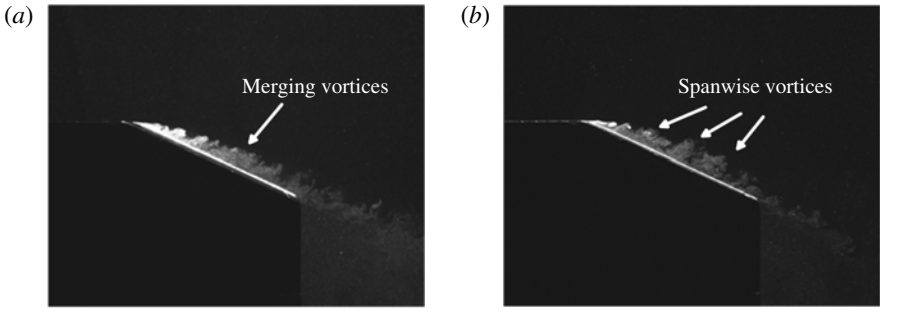


FIGURE 4. Typical photographs of the flow structure over the rear window in the (x, z) plane: (*a*) $y^* = 0$ (the symmetry plane); (*b*) $y^* = 0.36$. Flow is left to right.

figure 3*c*), where the C-pillar vortex is expected to occur. One minor peak is also discernible at $f^* = 0.53$, apparently the second harmonic of $St_r = 0.27$. Heft *et al.* (2011) reported at $Re = 9.0 \times 10^5$ a predominant vortex frequency of $St_r \approx 0.3$ near the side edge of the slanted surface based on surface pressure measurements. The deviation, albeit small, is probably due to a large difference in *Re*, *inter alia*, between the two investigations.

Figure 4 presents typical photographs captured from flow visualization in the planes of $y^* = 0$ and $y^* = 0.36$ over the rear window. The flow appears to separate at the upper edge of the rear window and then to reattach on the slant surface, forming a very small separation bubble (figure 4*a*), as shown in Lienhart & Becker's (2003) velocity measurements in the symmetry plane above the rear window. The shear layer appears to roll up behind this bubble (figure 4*a*,*b*). Kiya & Sasaki (1985) observed a similar rollup of the shear layer around a rectangular plate and linked this observation to the periodic enlargement and shrinking of the separation bubble. Thus formed vortices are probably responsible for the peak at $St_r = 0.20$ in E_u (figure 3*a*,*b*). Vortex merging is discernible at $y^* = 0$, as marked in figure 4(*a*), which corresponds spatially to the vanishing peak in E_u at A_4. Krajnović & Davidson (2005*a*) observed numerically the tilted vortices near the lateral sides of the slant, which tended to move towards the central region and merged with each other as convected downstream. They concluded that such vortex merging led to the hairpin vortices being destroyed with both legs broken.

In view of the strong three-dimensionality of the flow over the rear window, the hot-wire measurements were conducted at various spanwise locations. As illustrated in E_u (figure 5) measured along G_1–G_6 at $x^* = -0.51$ and $z^* = 0.86$, H_1–H_6 at $x^* = -0.17$ and $z^* = 0.79$, and I_1–I_6 at $x^* = 0$ and $z^* = 0.75$, the same predominant structures are captured, one at $St_r = 0.27$ near the side edge of the rear window ($y^* = 0.58$) and the other at $St_r = 0.20$. The latter is linked to spanwise vortices that occur behind the small separation bubble (figures 3 and 4). Evidently, the vortices occur over $y^* = 0$–0.36. It may be inferred that a quasi-periodic spanwise vortex roll is formed over the rear window, as proposed by Wang *et al.* (2013). There is a large variation in E_u from $y^* = 0.36$ to $y^* = 0.58$. It seems plausible that the spanwise vortices are suppressed under the effect of the C-pillar vortex near the side edge of the slant surface. The peak at $St_r = 0.20$ in E_u is most pronounced at $y^* = 0.36$ but becomes weaker and even vanishes when approaching $y^* = 0$ (figures 3 and 5). The spanwise vortices generated near the upper edge of the rear window are tilted, travelling downstream towards the central region of the slanted surface under the effect of the C-pillar vortex that grows

https://doi.org/10.1017/jfm.2015.332 Published online by Cambridge University Press

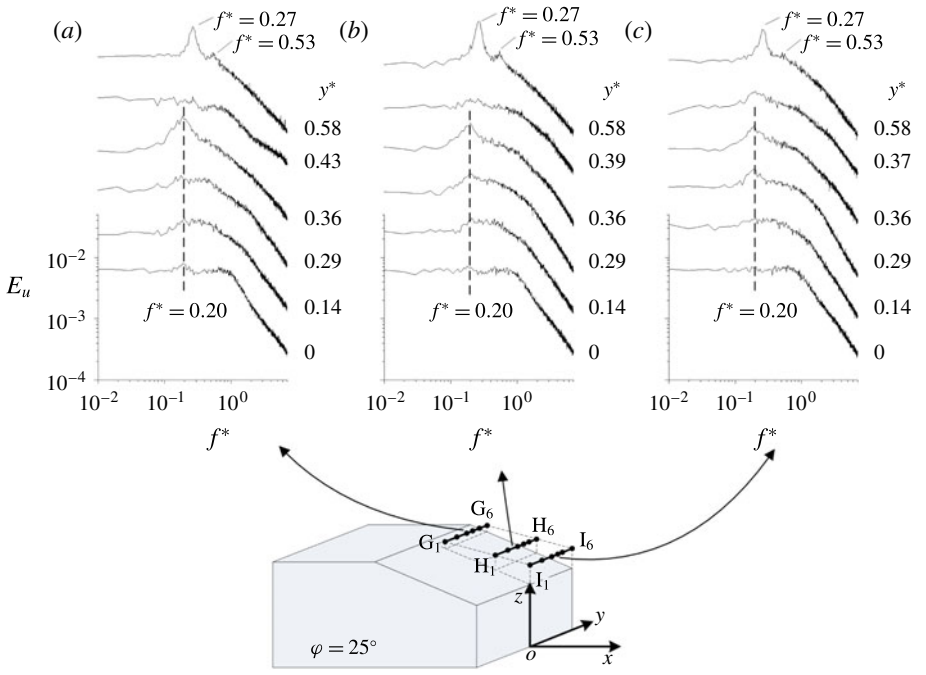


FIGURE 5. Power spectral density function E_u of the hot-wire signal measured along G_1–G_6 ($x^* = -0.51$, $z^* = 0.86$), H_1–H_6 ($x^* = -0.17$, $z^* = 0.79$), I_1–I_6 ($x^* = 0$, $z^* = 0.75$), respectively, over the slant surface.

downstream in size. The spanwise vortices in the central region are inclined to merge with each other and/or break up as convected downstream (Krajnović & Davidson 2005*a*).

3.2. *Longitudinal structure over the rear window*

Figure 6 presents typical instantaneous ω_x^* contours in the (y, z) plane at $x^* = 0.2$. The two most highly concentrated longitudinal vortices, marked by 'C', are the well-known C-pillar vortices. On the other hand, a number of alternately signed ω_x^* concentrations show up between the C-pillar vortices, which tend to be aligned in one row near the upper edge of the base, as enclosed by thick broken lines. Shabaka, Mehta & Bradshaw (1985) examined the evolution of a single longitudinal vortex embedded in a turbulent boundary layer. Their hot-wire-measured vorticity contours showed that the longitudinal vortex induced vorticity, whose sign was opposite to that of the primary vortex, in the region around the primary vortex. Logdberg, Fransson & Alfredsson (2009) investigated the evolution of a pair of longitudinal counter-rotating vortices in a turbulent boundary layer based on flow visualization and hot-wire measurements. They advocated that the vortex-induced vorticity, with an opposite sign to that of the primary vortex on the same side, rolled up into a secondary vortex outboard of the pair of primary vortices. As shown in figure 6, in the vicinity of each C-pillar vortex, there appears one relatively strong ω_x^* concentration, whose sign is opposite to that of the C-pillar vortex, with the maximum magnitude of ω_x^* reaching 7. In view of the induction effect of the two C-pillar vortices, this vorticity concentration is considered to be induced by the C-pillar vortex. For the same reason, the ω_x^* concentrations near

https://doi.org/10.1017/jfm.2015.332 Published online by Cambridge University Press

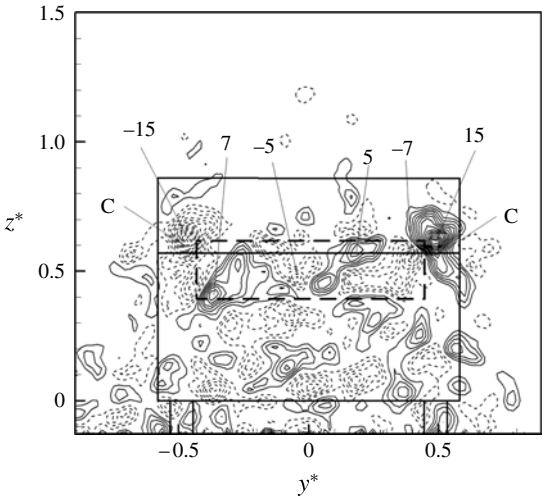


FIGURE 6. The PIV measurement of instantaneous streamwise vorticity ω_x^* contours in the (y, z) plane $x^* = 0.20$. The cutoff level is ± 1, and the contour increment is ± 1. The thick broken lines enclose a number of alternately signed ω_x^* concentrations formed between the C-pillar vortices.

the symmetry plane ($y^* = 0$), with their maximum magnitudes reaching 5, are probably induced by those secondary vortices.

3.3. *Flow structures behind the base*

Figure 7 presents E_u measured at different heights for a number of downstream stations behind the base in the plane of $y^* = 0$. At $x^* = 0.2$, which is within the recirculation bubble (e.g. Wang *et al.* 2013), E_u measured along K_1–K_6 is characterized by one prominent peak at $f^* = St_w = 0.44$ over $z^* = 0$–0.27. This peak is hardly discernible for $z^* > 0.36$. The spatial location where this peak is detected suggests that the unsteady flow structures associated with this peak may be linked to the recirculation bubbles behind the base. By $x^* = 0.4$ (L_1–L_6), this peak appears more pronounced and becomes evident for higher z^*, i.e. at $z^* = 0.36$, implying that the corresponding unsteady structures grow in strength and move upwards as advected downstream. By $x^* = 0.8$ (M_1–M_6), this peak can even be seen at $z^* = 0.54$. The unsteady structures appear fully grown and start to decay at larger x^*; the peak in E_u at $x^* = 1.4$ (N_1–N_6) is appreciably less prominent. The result is consistent with the numerical study by Minguez *et al.* (2008), who observed at $Re = 8.9 \times 10^5$ a predominant St of 0.49 near $x^* = 0.43$ and $z^* = 0$. The deviation in their St from our measurement is not unexpected in view of the possible boundary and other differences, besides Re, between the numerical and experimental studies. Based on the surface pressure tap measurements, Vino *et al.* (2005) observed a single predominant frequency at $St \approx 0.39$ at $y^* = 0$ on the upper ($z^* = 0.40$) and lower ($z^* = 0.13$) vertical base of an Ahmed model ($\varphi = 30°$, the high-drag configuration, $Re = (4.5$–$7.9) \times 10^5$), and a spectral phase shift of near π at this St between the pressure signals simultaneously measured at these two locations, that is, the two signals are out of phase. They thus proposed that the recirculation bubbles behind the vertical base behaved similarly to von Kármán vortex shedding from a

https://doi.org/10.1017/jfm.2015.332 Published online by Cambridge University Press

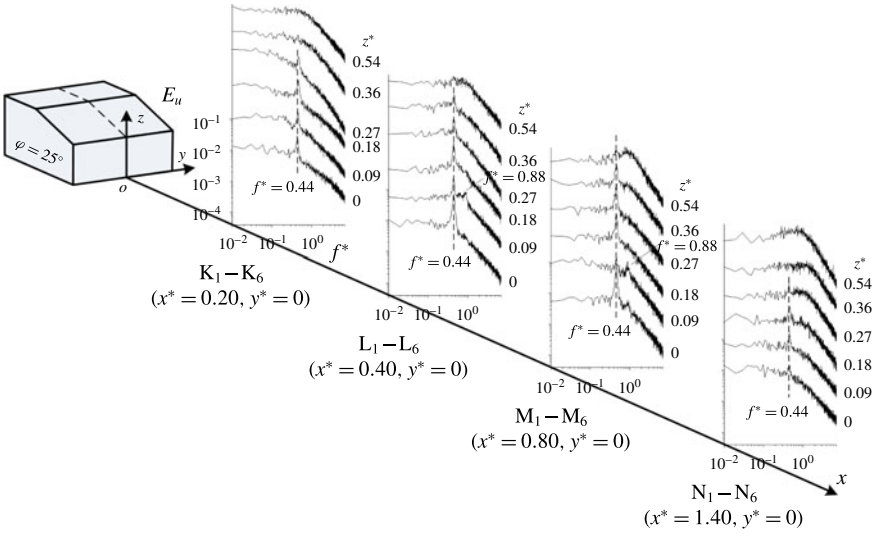


FIGURE 7. Power spectral density function E_u of the hot-wire signal measured along K_1–K_6, L_1–L_6, M_1–M_6, N_1–N_6, respectively, at $y^* = 0$ in the wake.

two-dimensional bluff body such as a square cylinder. It is worth commenting that the von Kármán vortex street is generated by the alternate separation of shear layers from the two trailing edges of a square cylinder (e.g. Alam, Zhou & Wang 2011). However, as shown later, the quasi-periodic structures at $St_w = 0.44$ result from the alternate emanation of fluid parcels from the upper and lower recirculation bubbles. One minor peak is also discernible at $f^* = 0.88$, the second harmonic of $St_w = 0.44$, at $x^* = 0.4$–0.8 for $z^* \leqslant 0.09$. This harmonic could not be seen at $x^* = 1.4$.

Typical flow structures captured from flow visualization are examined in figure 8 in order to obtain a better picture of how the unsteady structures at $St_w = 0.44$ are generated. At one instant, one structure is shed towards the ground from the upper recirculation bubble behind the base (figure 8*a*); at the other instant, another structure appears popping up from the lower recirculation bubble (figure 8*b*). The two distinct flow patterns are also observed from typical instantaneous ω_y^* contours measured in the symmetry plane ($y^* = 0$) of the wake, as illustrated in figure 8(*c*,*d*). The contours further indicate that the emanated structures, as enclosed by a thick contour, are associated with the concentrated vorticity. The fact that the two emanated structures are never seen to occur simultaneously suggests that the organized structures are produced alternately from the upper and lower recirculation bubbles, which are responsible for the pronounced peak at $St_w = 0.44$ and its second harmonic in E_u (figure 7). This is confirmed by the spectral phase shift $\Phi_{u_{L_1} u_{L_4}}$ of near π, i.e. out of phase, at $St_w = 0.44$ (figure 9*a*) between the hot-wire signals simultaneously obtained at L_1 ($z^* = 0$) and L_4 ($z^* = 0.27$). A similar observation on the spectral phase shift is also made at $x^* = 0.8$. However, the spectral phase shift $\Phi_{u_{N_1} u_{N_4}}$ at $St_w = 0.44$ between the hot-wire signals simultaneously obtained at N_1 ($z^* = 0$) and N_4 ($z^* = 0.27$) is near zero at $x^* = 1.4$, downstream of the recirculation bubbles (figure 9*b*). The observation will be explained later in this section.

One scenario is proposed for the observed unsteady structures at frequencies $St = 0.44$ and 0.88. The organized structures are shed alternately from the upper and lower recirculation bubbles, respectively, at a frequency of $St_w = 0.44$, as evidenced by the

https://doi.org/10.1017/jfm.2015.332 Published online by Cambridge University Press

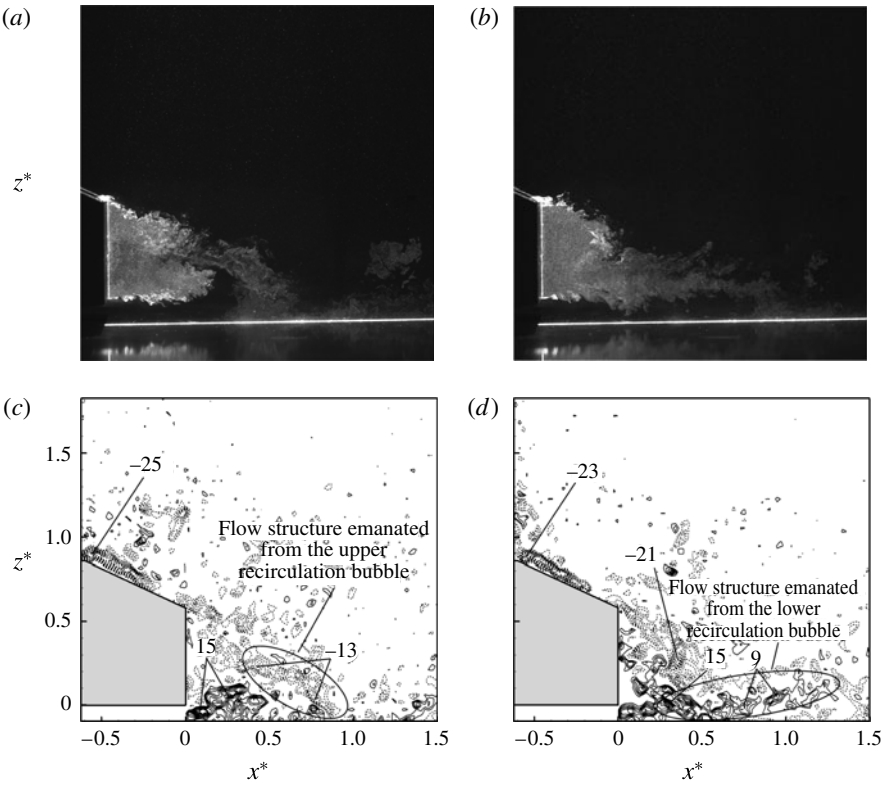


FIGURE 8. Typical instantaneous flow structure in the symmetry plane ($y^* = 0$) in the wake. (*a*,*b*) Flow visualization; the white line is the reflection of the laser light from the floor. (*c*,*d*) PIV-measured instantaneous spanwise vorticity ω_y^* contours; the cutoff level is ± 3, and the contour increment is ± 2.

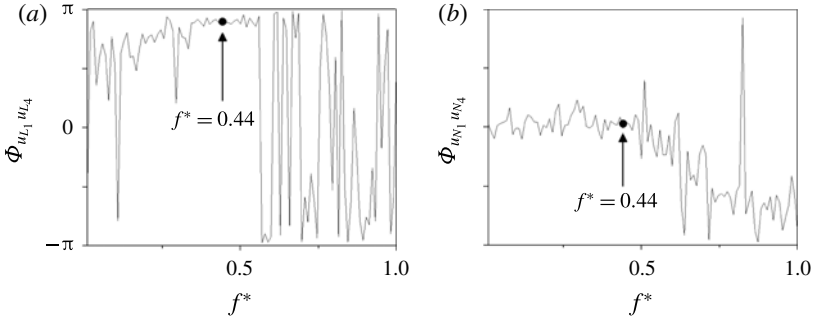


FIGURE 9. Spectral phase between hot-wire signals simultaneously measured at: (*a*) L_1 and L_4; (*b*) N_1 and N_4. Please refer to figure 7 for the locations of L_1, L_4, N_1 and N_4.

peak in E_u from $z^* = 0$ to 0.36 measured at $x^* = 0.4$ (figure 7) and a phase angle of near π at $St_w = 0.44$ in $\Phi_{u_{L_1} u_{L_4}}$ (figure 9*a*). The structure separated from the upper bubble sweeps towards the ground (figure 8*a*,*c*); on the other hand, the structure from the lower bubble is emanated upwards (figure 8*b*,*d*). Figure 8 indicates that the former structure appears short-lived, compared with the latter. This assertion is also consistent

https://doi.org/10.1017/jfm.2015.332 Published online by Cambridge University Press

with E_u measured over $x^* = 0.4$–1.4 (figure 7). A small portion of structures shed from the two bubbles may reach the same level of elevation over $x^* = 0.4$–0.8, as supported by the minor peak at $St = 0.88$ in E_u from $z^* = 0$ to 0.09 in this x^* range (figure 7). The structure separated from the upper bubble breaks up and disappears before reaching $x^* = 1.4$, and the peak shown in E_u at $x^* = 1.4$ is essentially the signature of structures emanated from the lower bubble. As such, $\Phi_{u_{N_1} u_{N_4}}$ is near zero at $St_w = 0.44$ (figure 9*b*). Vino *et al.* (2005) measured the turbulence intensity using a pressure probe in the (x, z) plane at $y^* = 0$ behind the vertical base of an Ahmed model, and observed that the upper recirculation bubble was stretched downstream towards the ground, on the one hand, and the lower bubble stretched downstream upwards, on the other. They advocated that vortex shedding behind the base was a process of alternating stretching of the upper and lower recirculation bubbles. Our proposed scenario provides an accurate account for the flow physical picture and an explanation for their stretched bubbles.

Since the quasi-periodic structures behind the vertical base of the Ahmed model show up with two distinct flow patterns, it could be insightful to extract these structures and characterize each of the two flow patterns. As illustrated in the instantaneous ω_y^* contours (figure 8*c,d*), the structures emanated from the upper and lower recirculation bubbles are characterized by relatively strong negative- and positive-vorticity concentrations, respectively. Therefore, we detect the occurrence of quasi-periodic structures based on their strength per unit area J^*, *viz.*

$$J^* = \frac{\iint_{S^*} \omega_y^* \, \mathrm{d}s^*}{S^*}, \tag{3.1}$$

where S^* is the area of a rectangular region of $x^* = 0.63$ to 0.85 and $z^* = -0.02$ to 0.11 in the symmetry plane ($y^* = 0$). The threshold for J^* is set at 2.0 after carefully checking detections against the plots of vorticity contours. Out of a total of 1200, 204 images with J^* values lower than -2.0 are identified with pattern 1, i.e. flow emanation from the upper recirculation bubble, and 216 with J^* values larger than 2.0 fall into the other flow pattern, or pattern 2. The ensemble averages are made for each pattern based on these detections. The dependence of $\delta = (\beta_N - \beta_{N-\Delta N})/\beta_N$ on N was calculated, where β denotes $\langle U \rangle$ and $\langle W \rangle$, and subscript N or $N - \Delta N$ is the number of images (ΔN is the increment in N). In this paper, angular brackets denote quantities ensemble-averaged based on the above described detections. The value of δ is estimated at the centre of the rectangular region (S^*) over which J^* is calculated. It has been found that δ converges rapidly, with increasing N, to within $\pm 3\,\%$ at $N \approx 200$ for $\langle U \rangle$ and $\langle W \rangle$ (not shown). Similar results have been obtained at other locations, thus indicating that the ensemble-averaged results from 204 (or 216) images are reasonably representative of flow features for each flow pattern.

The time-averaged sectional streamlines from the 1200 PIV-measured instantaneous images measured at $Re = 0.62 \times 10^5$ may allow us to determine the bubble or recirculation length, which is defined by the maximum longitudinal length of the wake bubble or reverse flow region, where $\overline{U} \leqslant 0$. The lengths of the upper and lower recirculation bubbles are $0.56\sqrt{A}$ and $0.53\sqrt{A}$, respectively, estimated from figure 10(*a*). One saddle point, marked by symbol '$\times$', occurs behind the recirculation bubbles. The ensemble-averaged sectional streamlines (figure 10*b*) based on the 204 images identified for pattern 1 exhibit a number of changes from the time-averaged streamlines (figure 10*a*).

https://doi.org/10.1017/jfm.2015.332 Published online by Cambridge University Press

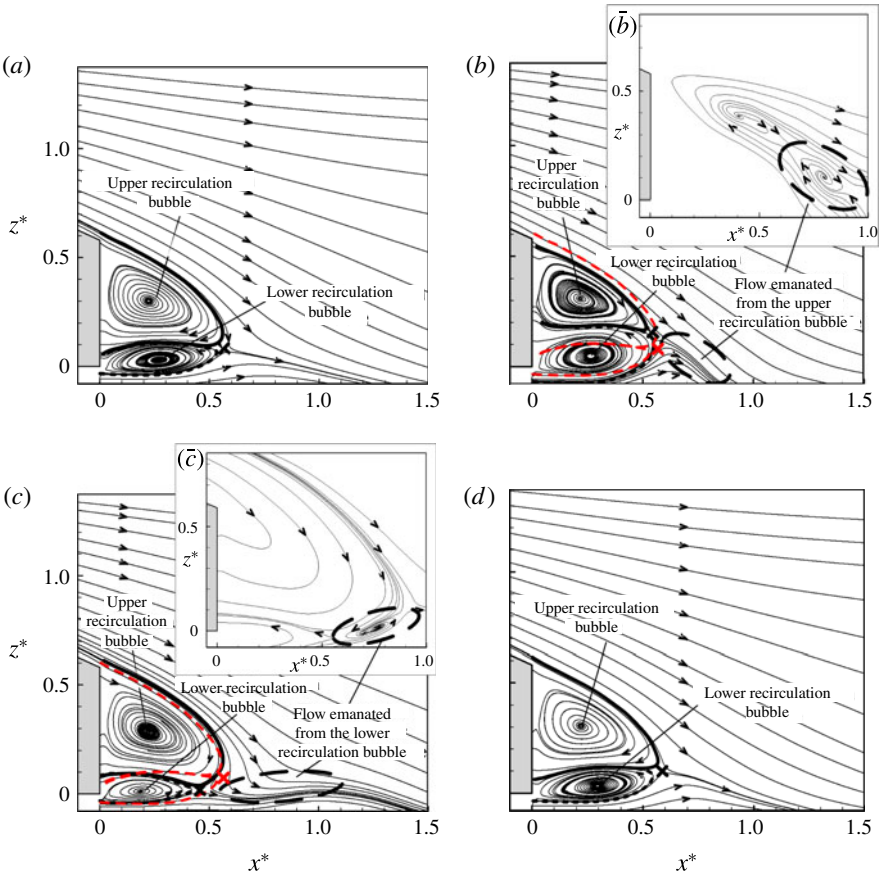


FIGURE 10. (Colour online) (*a*) Time-averaged sectional streamlines; (*b–d*) ensemble-averaged sectional streamlines; $(\bar{b}, \bar{c})$ ensemble-averaged sectional streamlines viewed in a reference frame convecting at (U_c^*, W_c^*). Symbol '×' denotes the saddle point. The red-coloured broken line in (*b*,*c*) indicates the bubble size, determined from time-averaged streamlines. $Re = 0.62 \times 10^5$.

Firstly, the streamlines (figure 10*b*) display a considerable downsize of the upper recirculation bubble but an expanded lower bubble, as compared with their time-averaged counterpart (figure 10*a*). To facilitate data interpretation, the recirculation bubbles and the saddle point, shown in the time-averaged sectional streamlines, are indicated by a broken curve and symbol '×' in red (figure 10*b*), respectively. The upper bubble is $0.51\sqrt{A}$ in longitudinal length, appreciably shorter than its time-averaged counterpart, $0.56\sqrt{A}$ (figure 10*a*), whereas the lower bubble becomes $0.55\sqrt{A}$, longer than that ($0.53\sqrt{A}$) in figure 10(*a*). The saddle point is also shifted, compared with that in figure 10(*a*). Downstream of the saddle point, one structure separated from the upper recirculation bubble, as highlighted by a thick broken line, is seen to sweep towards the ground. This structure is closely connected to the change in bubble size and saddle point position, which have a significant impact on the base pressure of an Ahmed model. In their numerical simulation on active drag control of an Ahmed model ($\varphi = 25°$, $Re = 8.9 \times 10^5$), Wassen & Thiele (2008) deployed streamwise steady blowing along the upper and two side edges of the rear window, and the lower and two side edges of the base. Their

https://doi.org/10.1017/jfm.2015.332 Published online by Cambridge University Press

calculated time-averaged streamlines in the symmetry plane of the wake showed that both upper and lower recirculation bubbles were considerably enlarged longitudinally under control. Meanwhile, the saddle point behind the bubbles was pushed farther downstream. Accordingly, the time-averaged base pressure increased by 14 %. In his numerical simulation in the wake of an Ahmed model ($\varphi = 25°$), Krajnović (2014) deployed one array of finite-length circular cylinders, upstream of the upper edge of the rear window, for drag reduction. The lengths of the two bubbles behind the base were elongated, associated with a significant drag reduction by 11.6 %.

Secondly, a vortical structure occurs downstream of the saddle point, as shown in figure 10($\bar{b}$). The structure emanated from the upper bubble is characterized by a relatively strong vorticity concentration of negative sign, as evidenced by the instantaneous ω_y^* contours (figure 8*c*). This concentration however is hardly recognizable in figure 10(*b*). This is because a vortex is in general only visible in streamlines when viewed from a reference frame convecting with the same velocity as the vortex centre (e.g. Zhou & Antonia 1994). Note that vortices may change in location from one PIV snapshot to another. As such, we screened carefully the 204 PIV snapshots identified as pattern 1 and picked up 31 images whose maximum ω_y^* concentrations, associated with the emanated structures, occurred at approximately the same location, i.e. $(x^*, z^*) = (0.79, 0.1)$. Using the velocity (U_c^*, W_c^*) at this location as that at which the reference frame is convected, then the velocity components U_r^* and W_r^* of the 31 images are determined by

$$U_r^* = U^* - U_c^*, \tag{3.2}$$

$$W_r^* = W^* - W_c^*. \tag{3.3}$$

Ensemble-averaged sectional streamlines (figure 10$\bar{b}$) for this group of data then display a different flow topology, as in figure 10(*b*). Two foci occur at $(x^*, z^*) = (0.4, 0.39)$ and $(0.79, 0.1)$, respectively. The former is due to the upper recirculation bubble, whose centre deviates from that in figure 10(*b*) because of different vortex convection velocities used in the calculation of streamlines, and the latter to the vortical structure emanated from this bubble.

The ensemble-averaged data based on the detections of pattern 2 show considerable differences. The sectional streamlines (figure 10*c*) display an upper recirculation bubble significantly larger than the lower bubble. This result, along with that shown in figure 10(*b*), suggests that the bubble, be it upper or lower, reduces considerably in size as a result of a fluid parcel ejected from it. Furthermore, a change occurs in the position of the saddle point, which is shifted upstream and meanwhile closer to the ground, compared with that shown in figure 10(*b*) and that in figure 10(*a*). Behind the saddle point, one structure is seen to rebound downstream from the lower recirculation bubble, as enclosed by a thick broken line. As indicated by the instantaneous ω_y^* contours (figure 8*d*), this structure is characterized by a relatively strong positive-vorticity concentration. But the streamlines (figure 10*c*) do not show the presence of a vortical structure corresponding to this concentration. Similarly to the analysis of pattern 1, we examined the 216 PIV snapshots detected for pattern 2 and selected 39 where the maximum ω_y^* concentration of the emanated structure occurs at approximately the same location of $(x^*, z^*) = (0.77, 0.02)$. With the reference frame fixed at this location, we may recalculate the ensemble-averaged sectional streamlines based on the 39 snapshots. As shown in figure 10($\bar{c}$), one focus

https://doi.org/10.1017/jfm.2015.332 Published online by Cambridge University Press

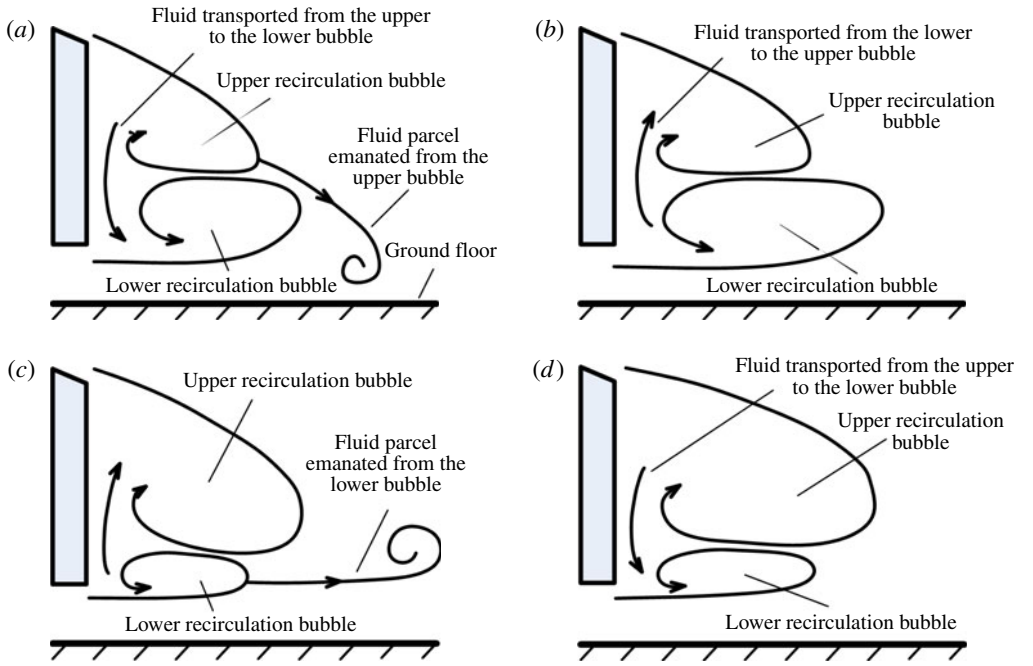


FIGURE 11. Schematic of the physical process for the pulsation of two recirculation bubbles and the generation of a quasi-periodic flow structure.

occurs at $(x^*, z^*) = (0.77, 0.02)$, indicating the structure separated from the lower bubble.

Ensemble averaging has also been performed based on the remaining 780 PIV snapshots, excluding those identified for patterns 1 and 2. The lengths of the upper and lower recirculation bubbles in the ensemble-averaged streamlines are approximately $0.57\sqrt{A}$ and $0.54\sqrt{A}$ (figure 10*d*), respectively, nearly the same as those in the time-averaged streamlines (figure 10*a*).

In their experimental study on flow around a rectangular plate, Kiya & Sasaki (1985) found that flow separated from the leading edge and then reattached downstream, forming a separation bubble. This bubble was characterized by periodic enlargement and shrinkage, i.e. bubble pulsation, and the shear layer rolled up behind the bubble, forming vortices. Tafti & Vanka (1991) studied numerically the mechanism causing bubble pulsation and conjectured that the bubble expanded as a result of entrainment of fluid from the free stream, which caused a gradual rise in pressure within the bubble. The bubble eventually burst when its pressure reached a certain level, which was associated with an outward movement of fluid in the spanwise direction and the emanation of vortices downstream from the bubble. Enlightened by these studies, we propose a physical process for the growing and shrinking recirculation bubbles and the alternate emanation of fluid structures from the two bubbles based on the present observations.

The entire process may be divided into four phases, as schematically shown in figure 11.

Phase A. The flow separated from the upper edge of the model base is entrained into the upper recirculation bubble, resulting in a gradual increase in pressure within the

https://doi.org/10.1017/jfm.2015.332 Published online by Cambridge University Press

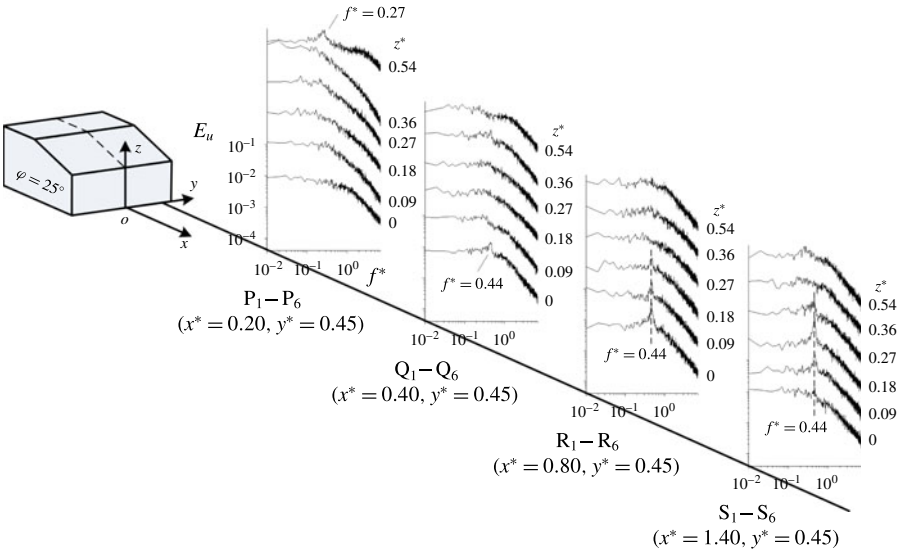


FIGURE 12. Power spectral density function E_u of the hot-wire signal measured along P_1–P_6, Q_1–Q_6, R_1–R_6, S_1–S_6, respectively, at $y^* = 0.45$ in the wake.

bubble. When the pressure reaches a certain level, the bubble cannot sustain it any more and then collapses. As a result, a structure is emanated towards the ground from the bubble, accompanied by a substantially reduced size of the bubble, as evident in the ensemble-averaged streamlines of pattern 1 (figure 11*b*). Meanwhile, part of the fluid in the upper bubble is transported into the lower bubble, as indicated by instantaneous velocity vectors (not shown), due to a pressure differentiation between the two bubbles.

Phase B. After the collapse of the upper bubble, the flow separated from the lower edge of the model base is entrained into the lower recirculation bubble. As such, the pressure within this bubble rises and then exceeds that of the upper bubble, resulting in the movement of fluid from the lower to the upper bubble.

Phase C. The lower bubble continues its rise in size and pressure until its collapse, associated with a sudden downsize and the emanation of a structure from it, as observed in ensemble-averaged sectional streamlines of pattern 2 (figure 10*c*). The transport of fluid from the lower to the upper bubble is also evident in the instantaneous velocity vectors (not shown).

Phase D. The upper bubble gradually expands in size and rises in pressure. Part of its fluid will move into the lower bubble once its pressure is higher. At an adequately high pressure, the bubble bursts, which starts the next cycle of bubble pulsation and alternate emanation of structures.

In order to gain insight into the three-dimensionality of unsteady flow structures, the hot-wire measurements were conducted in the (x, z) plane of $y^* = 0.45$ for a number of downstream locations. The E_u plot (figure 12) displays no peak at $x^* = 0.2$ over $z^* = 0$–0.36 (P_1–P_5). But at $z^* = 0.54$ (P_6) one peak is discernible at $f^* = St_s = 0.27$, where the C-pillar vortex occurs. At $x^* = 0.4$, a small peak at $St_w = 0.44$ is identifiable at Q_1 ($z^* = 0$) near the ground. This peak grows and propagates to higher

https://doi.org/10.1017/jfm.2015.332 Published online by Cambridge University Press

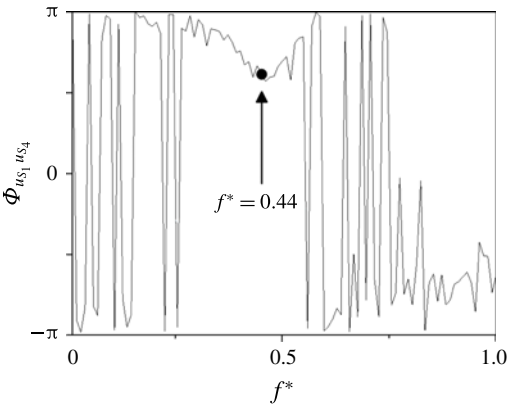


FIGURE 13. Spectral phase between hot-wire signals simultaneously measured at S_1 and S_4. Please refer to figure 12 for the locations of S_1 and S_4.

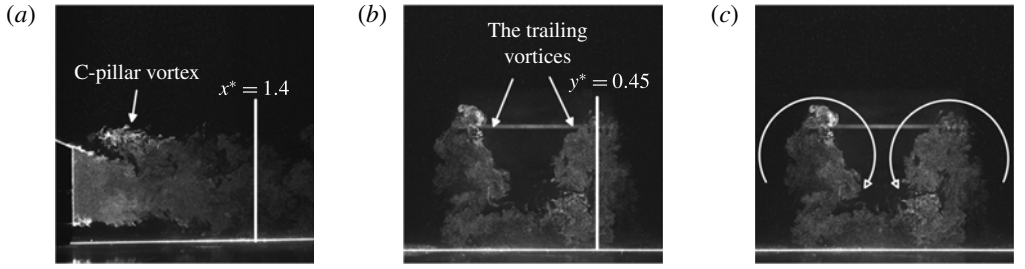


FIGURE 14. Typical photographs of the flow structure of the wake (flow is left to right): (*a*) in the (x, z) plane ($y^* = 0.45$); (*b*) in the (y, z) plane ($x^* = 1.4$), $t = t_0$ (arbitrary); (*c*) $t = t_0 + 120$ μs. The white line results from the reflection of the laser light from the floor.

z^* with increasing x^*, as observed in the symmetry plane (figure 7). A comparison between figures 7 and 12 indicates that the unsteady flow structures at $St_w = 0.44$ are formed initially about the symmetry plane behind the base. With increasing x^*, they move upwards and grow in both strength and spanwise extent. As shown in figure 13, $\Phi_{u_{S_1}u_{S_4}}$ between two hot-wire signals measured at S_1 and S_4 in the (x, z) plane of $y^* = 0.45$ ($x^* = 1.4$) is near $\pi/2$ at $St_w = 0.44$ (figure 12). This phase shift, neither near π nor near zero, is probably due to strong interactions between the C-pillar vortex and the unsteady structure, as indicated by flow visualization in the plane of symmetry (figure 8) and also in the lateral plane, shown below.

Figure 14(*a*) presents a typical photograph of flow visualization captured in the (x, z) plane of $y^* = 0.45$. The wake is characterized by the alternate emanation of fluid structures from the upper and lower recirculation bubbles in the symmetry plane (figure 8*a*,*b*) and exhibits an upward growth in the (x, z) plane of $y^* = 0.45$, merging into the C-pillar vortex that occurs above the upper recirculation bubble (figure 14*a*). The result is internally consistent with the fact that the peak at $St_w = 0.44$ does not show up in E_u for $z^* > 0.27$ in the near wake (figure 12), obtained in the same plane. It also conforms to Ahmed *et al.*'s (1984) observation based on the cross-flow velocity measurement, that is, the C-pillar vortices interact with the upper recirculation bubble

https://doi.org/10.1017/jfm.2015.332 Published online by Cambridge University Press

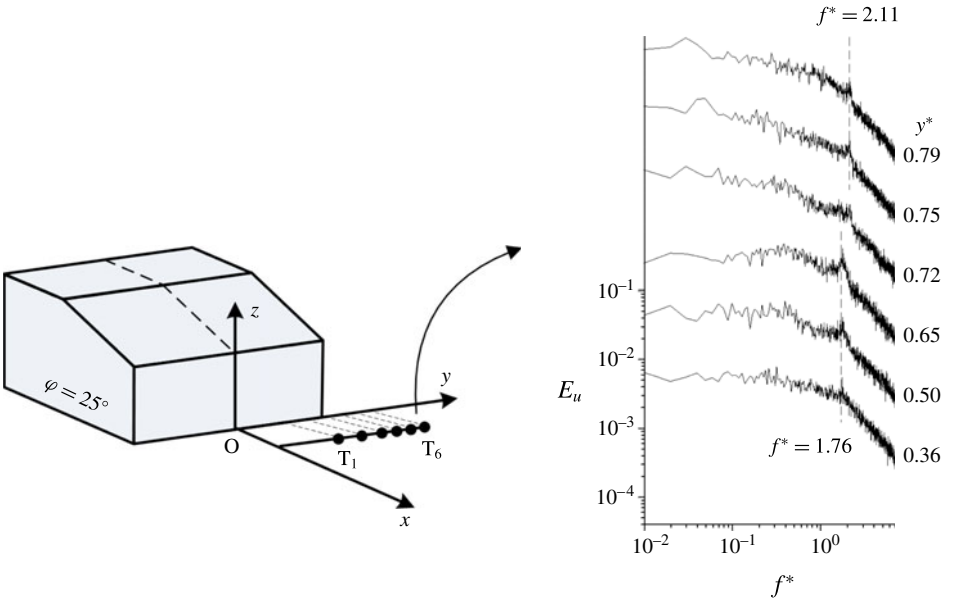


FIGURE 15. Power spectral density function E_u of the hot-wire signal measured along T_1–T_6 ($x^* = 0.09$, $z^* = 0$) in the wake.

between $x^* = 0.24$ and 0.60 and then form one pair of counter-rotating trailing vortices in the wake. Figure 14(*b*,*c*) shows photographs from flow visualization in the (y, z) plane at $x^* = 1.4$, which is normal to the mean flow direction. One pair of trailing vortices occurs. By comparing two sequential photographs captured at a time interval of 120 μs, we may determine that the two vortices are counter-rotating, as shown by the arrows in figure 14(*c*). There is a downwash flow in the central region near $y^* = 0$ induced by the two counter-rotating vortices, as observed from the measured cross-flow velocity distributions in the plane of $x^* = 1.49$ by Lienhart & Becker (2003). Note that the peak at $St_w = 0.44$ in E_u becomes more pronounced at $x^* = 1.4$ along S_1–S_4 (figure 12), away from the symmetry plane, than its counterpart along N_1–N_4 in the symmetry plane (figure 7). The observation agrees with Lienhart & Becker's (2003) measurement of the turbulent kinetic energy in the (y, z) plane of $x^* = 1.49$, which appeared larger away from the symmetry plane.

Hot-wire measurements were conducted along T_1–T_6 ($x^* = 0.09$, $z^* = 0$) behind the lower edge of the vertical base to capture possible quasi-periodic structures generated in the gap between the floor and the model's underside. The E_u plot (figure 15) displays two major peaks. One occurs at $f^* = St_l = 2.11$ over $y^* = 0.75$–0.79. Wang *et al.*'s (2013) PIV measurements in the (y, z) plane of $x^* = 0.2$ ($Re = 6.2 \times 10^4$) showed one vortex near the lower corner of the Ahmed model ($\varphi = 25°$) at $(y^*, z^*) \approx (\pm 0.72, -0.01)$, which they referred to as the lower vortex. This coincidence in the location of y^* and z^* does not necessarily suggest a link between the peak at $St_l = 2.11$ and the lower vortex. It has been confirmed that the unsteady structures of $St_l = 2.11$ result from vortex shedding from the cylindrical struts located at $x^* = -2.52$ and $y^* = \pm 0.49$ between the model underside and the floor, which will be discussed in § 4. The other peak occurs at $f^* = St_g = 1.76$ over $y^* = 0.36$–0.65, corresponding spatially to the gap vortex identified by Wang *et al.* (2013). Note that this St_g corresponds to a dimensionless frequency $St_D \approx 0.16$ based on U_∞ and the

https://doi.org/10.1017/jfm.2015.332 Published online by Cambridge University Press

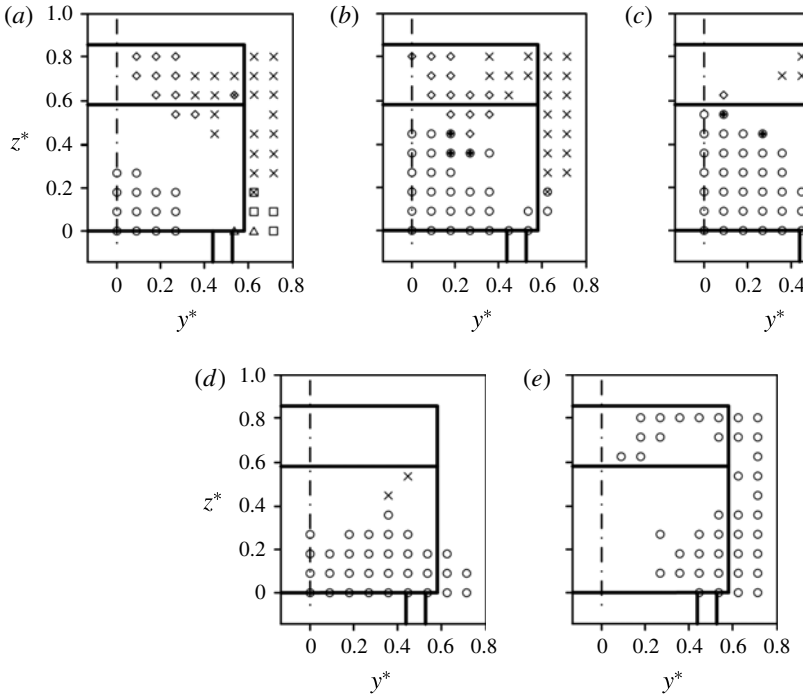


FIGURE 16. Locations where the predominant vortex frequency is detected in the (y, z) plane: (*a*) $x^* = 0.2$; (*b*) 0.4; (*c*) 0.8; (*d*) 1.4; (*e*) 2.2. Symbols: ◇, $St_r = 0.20$; ×, $St_s = 0.27$; ○, $St_w = 0.44$; △, $St_g = 1.76$; □, $St_l = 2.11$. Symbols ⟐, ◈, ⊗ and ☒ denote the simultaneous occurrence of two frequencies, i.e. St_r and St_s, St_r and St_w, St_s and St_w, and St_s and St_l, respectively.

diameter D of the cylindrical strut between the model underside and floor, which is close to the Strouhal number, 0.20, in a circular cylinder wake. The discrepancy is probably due to the effect of the boundary layer in the gap, which reduces the actual fluid speed and hence St_D (e.g. Krajnović & Davidson 2005*b*; Wang, Zhou & Mi 2012). It may be inferred that the peak at $St_g = 1.76$ is probably associated with the gap vortices generated by the struts located at $x^* = -1.11$ and $y^* = \pm 0.49$.

3.4. *The spatial extent of identified unsteady structures*

Five distinct vortex frequencies are now identified over the rear window and behind the vertical base, i.e. St_r, St_s, St_w, St_g and St_l. The locations where they are detected in the (y, z) plane vary for different downstream stations. Figure 16 presents their spatial distributions in the (y, z) plane at $x^* = 0.2$, 0.4, 0.8, 1.6 and 2.2. The Strouhal number St_i, where $i \in \{r, s, w, g, l\}$, is considered to occur provided that the ratio of the Hertz-averaged energy in E_u over $St \in [St_i - 0.01; St_i + 0.01]$ to that over $St \in [St_i - 0.15; St_i + 0.15]$ exceeds 1.3, at which a pronounced peak can be seen at St_i in E_u.

At $x^* = 0.2$ (figure 16*a*), the St_r associated with the spanwise vortices occurs mainly in the central region above $z^* = 0.54$, but is not detected in the plane of symmetry. At $x^* = 0.4$, the unsteady structure corresponding to St_r spreads slightly over a larger y^* and lower z^*, even discernible at $z^* = 0.36$ (figure 16*b*). Ahmed *et al.* (1984) observed a downwash flow in the central region near $y^* = 0$ induced by the

https://doi.org/10.1017/jfm.2015.332 Published online by Cambridge University Press

two counter-rotating C-pillar vortices based on cross-flow velocity measurement at $x^* = 0.24$ and 0.60. Under the effect of the downwash flow, spanwise vortices formed over the rear window may move downwards as convected downstream, accounting for the downward extension of the St_r region. However, this frequency can be hardly detected by $x^* = 0.8$.

The St_s value is captured over a relatively large area about the side edge of the rear window and the base, coinciding approximately with the expected location of the C-pillar vortex. The area of its occurrence changes only slightly at $x^* = 0.4$ but shrinks greatly at $x^* = 0.8$. By $x^* = 1.4$, this frequency is barely detectable.

The St_w value due to the quasi-periodic structures emanated from the recirculation bubbles is observed at $x^* = 0.2$ in the central region ($y^* = 0$–0.27) behind the lower base ($z^* < 0.3$). With increasing x^*, the area of its occurrence grows rather rapidly in both y^* and z^* directions until reaching $x^* = 0.8$ (figure 16*a–c*). At the same time, the corresponding unsteady structures grow in strength, as evident in figures 7 and 11. At $x^* = 1.4$ (figure 16*d*), the height at which this frequency is detected drops substantially to $z^* < 0.3$, resulting from the breakup of the structure emanated downwards from the upper recirculation bubble due to its interaction with the ground, which is supported by the flow visualization photograph of the structure (figure 8*a*). This result also explains why $\Phi_{u_{N_1}u_{N_4}}$ at $St_w = 0.44$ is near zero at $x^* = 1.4$ (figure 9*b*). However, at $x^* = 2.2$ (figure 16*e*) this frequency is detected again beyond $z^* = 0.3$, which is probably attributed to interactions between the trailing vortices and the flow structure emanated from the recirculation bubbles.

The St_g and St_l values are detected at $x^* = 0.2$. The former occurs at the right lower corner of the base, which is ascribed to the gap vortex, and the latter coincides spatially with the lower vortex (Wang *et al.* 2013). By $x^* = 0.4$, they both disappear.

4. Origin of the unsteady flow structures

Experimental data have uncovered five distinct Strouhal numbers, i.e. $St_r = 0.20$ and $St_s = 0.27$ over the rear window, and $St_w = 0.44$, $St_g = 1.76$ and $St_l = 2.11$ behind the vertical base. As discussed previously, the unsteady structures of $St_w = 0.44$ originate from the alternate emanation of structures from the upper and lower recirculation bubbles, and those of $St_g = 1.76$ correspond spatially to the gap vortices, which are generated by the struts located at $x^* = -1.11$ and $y^* = \pm 0.49$ between the model underside and the ground floor. What, then, are the origins of the other three?

One naturally goes upstream to search for possible solutions. Figure 17 presents E_u measured along D_1–D_5 ($x^* = -2.33$, $z^* = 0.95$) and F_1–F_5 ($x^* = -1.27$, $z^* = 0.95$) above the roof, downstream of the leading edge. A pronounced peak occurs at $f^* = St_r = 0.20$ in the symmetry plane ($y^* = 0$) and also over $y^* = 0.29$–0.36 (figure 17*a*). Minguez *et al.* (2008) found numerically at $Re = 8.9 \times 10^5$ that flow separated and then reattached near the leading edge of the roof, producing a recirculation bubble periodically pulsating at $St = 0.174$. Based on flow visualization at $Re = 9.3 \times 10^3$ in a water tunnel, Spohn & Gillieron (2002) observed vortices at $St \approx 2.64$ emanated from the separation region near the leading edge in the plane of symmetry. They also noted one pair of counter-rotating longitudinal vortices, originating from two foci at each end of the separation line. Furthermore, the flow separation region pulsated at a frequency of 0.21 Hz or $St \approx 0.2$ if normalized by $\sqrt{A}$. Note that E_u measured over $y^* = 0.14$–0.22 displays its predominant peak at $f^* = St_a = 0.14$, considerably smaller than St_r ($= 0.2$). This peak is spatially close to the longitudinal vortex core at (y^*, z^*) $\approx$ (0.20, 0.93), as shown in Spohn &

https://doi.org/10.1017/jfm.2015.332 Published online by Cambridge University Press

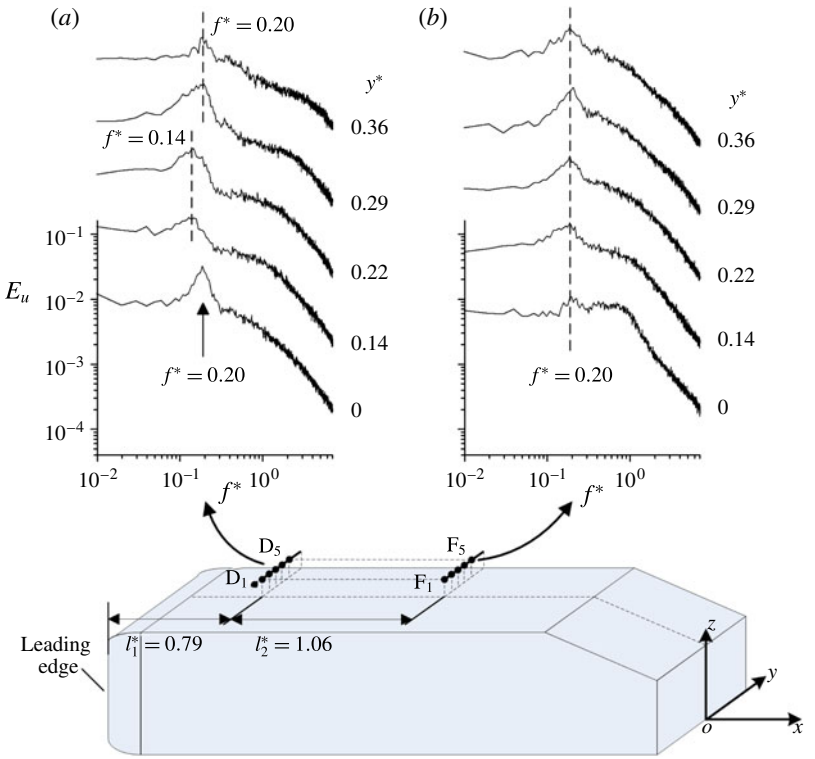


FIGURE 17. Power spectral density function E_u of the hot-wire signal measured along (*a*) D_1–D_5 ($x^* = -2.33$, $z^* = 0.95$) and (*b*) F_1–F_5 ($x^* = -1.27$, $z^* = 0.95$), respectively, above the roof.

Gillieron's (2002) flow visualization photograph in the (y, z) plane of $x^* = -2.34$. The observation bears similarity to that made by Kiya & Sasaki (1985) in flow around a blunt flat plate. They found that flow separated from the leading edge and then reattached downstream, forming a separation bubble, and vortices were generated downstream of the bubble at a frequency of $0.65U_\infty/x_R$ (x_R is the bubble length). It is therefore plausible that the peak at $St_a = 0.14$ in E_u is linked to the oscillation of the longitudinal vortex core originated from bubble pulsation.

Further downstream at $x^* = -1.27$, E_u displays only one pronounced peak at $St_r = 0.20$, the peak at $St_a = 0.14$ disappearing (figure 17*b*) due to the weakened longitudinal vortex as advected downstream. The peak at $St_r = 0.20$ measured along F_1–F_5 ($x^* = -1.27$) suggests that vortices generated near the leading edge persist downstream, which does not support Ahmed *et al.*'s (1984) proposition that the flow interference between the rear end and the fore-body was weak due to a relatively long midsection. More evidence will be provided later in this section. A hump occurs at $f^* \approx 0.84$ in E_u measured at $y^* = 0$ (figure 17*b*), probably related to the shear layer instability developed over the roof.

The fact that the unsteady structures detected over the rear window at $y^* = 0$–0.36 (figures 3 and 5) occur at the same frequency ($St_r = 0.20$) as those above the roof (figure 17) suggests a connection between them. The spectral coherence $Coh_{u_\beta u_\gamma}$ ($\equiv (Co^2_{u_\beta u_\gamma} + Q^2_{u_\beta u_\gamma})/E_{u_\beta}E_{u_\gamma}$) is thus examined, where signals u_β and u_γ were simultaneously measured using two single hot wires, one placed above the roof

https://doi.org/10.1017/jfm.2015.332 Published online by Cambridge University Press

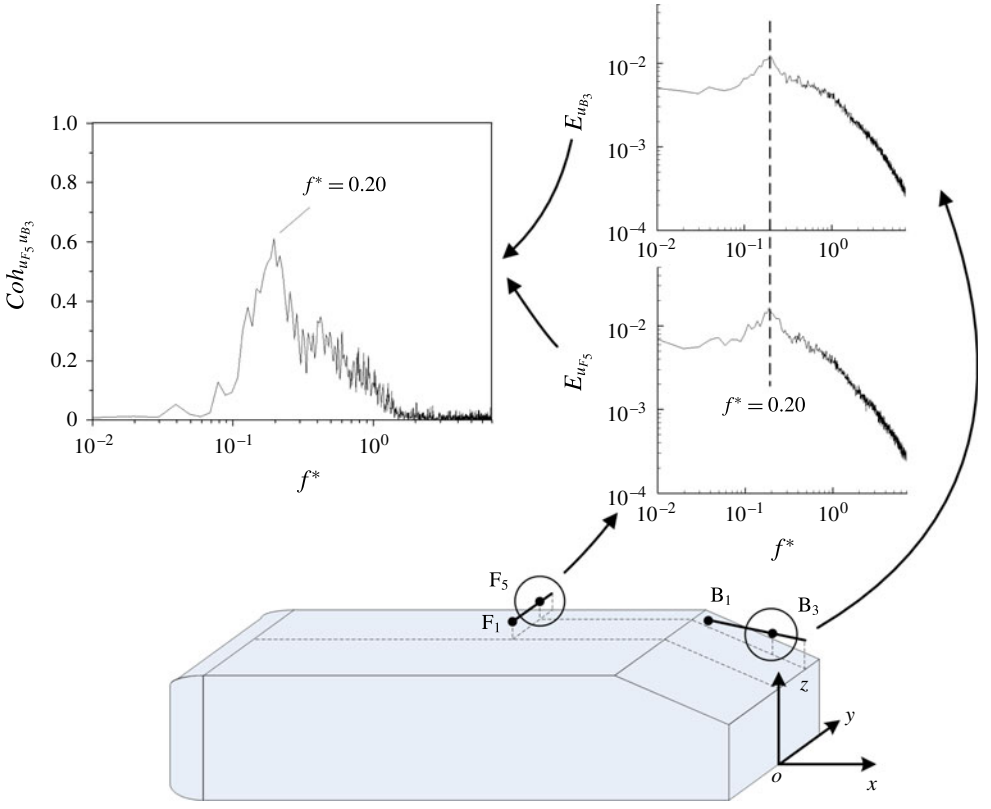


FIGURE 18. Spectral coherence between simultaneously measured hot-wire signals u_{F_5} and u_{B_3}. Please refer to figures 3 and 17 for the locations of B_3 and F_5.

and the other over the rear window, and $Co_{u_\beta u_\gamma}$ and $Q_{u_\beta u_\gamma}$ are the cospectrum and quadrature spectrum of u_β and u_γ, respectively. The coherence $Coh_{u_\beta u_\gamma}$ provides a measure for the quantitative correlation between the spectral components of u_β and u_γ (Antonia, Zhou & Matsumara 1993). As illustrated in figure 18, both $E_{u_{\beta_3}}$ and $E_{u_{F_5}}$ of u_{F_5} and u_{B_3}, measured at F_5 and B_3, respectively, display a predominant peak at the same frequency ($St_r = 0.20$). The $Coh_{u_{F_5}u_{B_3}}$ value shows a pronounced peak, reaching 0.63, at $f^* = St_r = 0.20$, indicating an excellent correlation between u_{F_5} and u_{B_3} at this frequency. The observation points to the fact that the shear layer development above the roof has a significant effect on flow separation and even vortex shedding from the slanted rear window. In fact, it may be concluded that the frequency of vortex shedding from the rear window is dictated by that of vortices generated behind the bubble near the leading edge of the roof.

The above finding prompts us to look at the shear layer developed over the side surface of the model. Figure 19 presents E_u measured along E_1–E_5 ($x^* = -1.27$, $y^* = 0.63$) near the side face. A pronounced peak occurs at $f^* = St_l = 2.11$ at E_1 near the ground ($z^* = 0.14$). This predominant frequency is the same as that ($St_l = 2.11$) identified in E_u measured at T_5 and T_6 (figure 15). Note that this St_l corresponds to a dimensionless frequency of $St_D \approx 0.19$ and is approximately equal to the Strouhal number (≈ 0.20) in the wake of a circular cylinder. It may be inferred that the St_l is the frequency of vortices generated by the struts located at $x^* = -2.52$ and $y^* = \pm 0.49$ between the model underside and the floor.

https://doi.org/10.1017/jfm.2015.332 Published online by Cambridge University Press

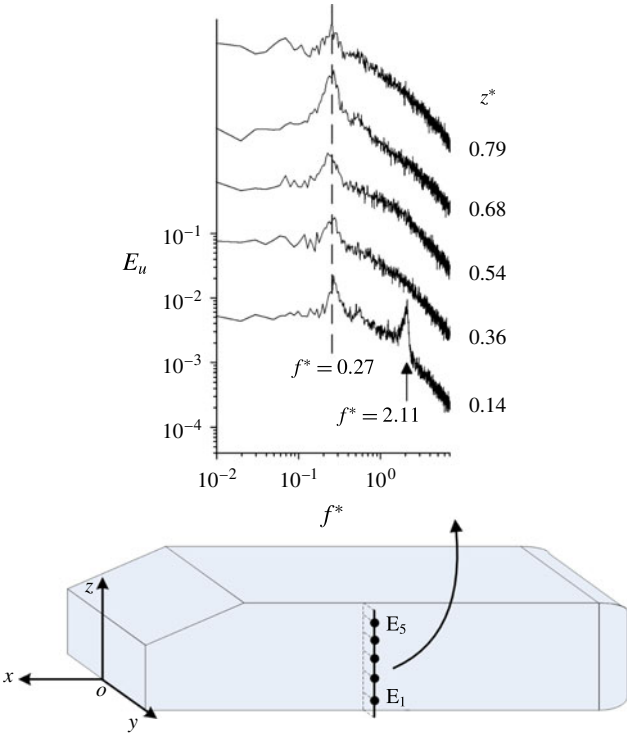


FIGURE 19. Power spectral density function E_u of the hot-wire signal measured along E_1–E_5 ($x^* = -1.27$, $y^* = 0.63$) near the side surface.

Another predominant peak occurs at $f^* = St_s = 0.27$ over $z^* = 0.14$–0.79. Grandemange, Gohlke & Cadot (2013) studied the flow around a square-back Ahmed body ($\varphi = 0°$) at $Re = 1.1 \times 10^5$ based on the surface pressure measurements in the (x, y) plane at $z^* = 0.43$. They observed that the flow separated and then reattached near the leading edge of the side face, forming a recirculation bubble located roughly at $-3.0 < x^* < -2.6$. Like the hairpin vortex observed above the roof, the side vortex is a structure emanated from the recirculation bubble that occurs near the leading edge of the side face. Since the predominant unsteady structures at $St_s = 0.27$ are detected along the side edge of the rear window and over the side surface, we used two hot wires to measure simultaneously the flow at E_4 and C_3 (figure 20). The spectral coherence $Coh_{u_{E_4}u_{C_3}}$ between u_{E_4} and u_{C_3}, obtained at E_4 and C_3, respectively, shows a pronounced peak, with its magnitude reaching 0.92, at $f^* = St_s = 0.27$, indicating a near perfect correlation between u_{E_4} and u_{C_3} at this frequency. It is evident that the vortex frequency $St_s = 0.27$ detected along the side edge of the slant surface is dictated by that of the side vortices formed over the side face of the Ahmed model.

5. Reynolds number effect

The *Re* effect on the flow has not been well addressed in the literature. The Ahmed model is designed to minimize flow separation from its fore-body and to have fixed flow separation from its after-body, which is characterized by clearly defined corners. Nevertheless, Minguez *et al.*'s (2008) LES at $Re = 8.9 \times 10^5$ showed that flow separated at the fore-body and then reattached on the roof and lateral sides,

https://doi.org/10.1017/jfm.2015.332 Published online by Cambridge University Press

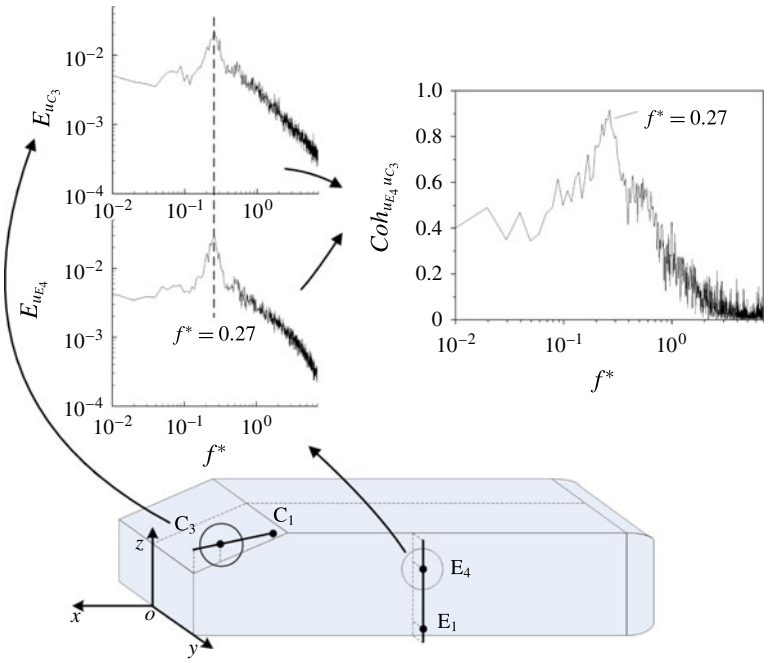


FIGURE 20. Spectral coherence between simultaneously measured hot-wire signals u_{E_4} and u_{C_3}. Please refer to figures 3 and 19 for the locations of C_3 and E_4.

forming a bubble. The observation suggests a dependence of the flow structure on *Re*. Previously reported drag coefficient and Strouhal number data also display a variation with different *Re* (e.g. Vino *et al.* 2005; Thacker *et al.* 2010; Joseph *et al.* 2012). In this section, we will examine the possible dependence on *Re* of the Strouhal numbers based on hot-wire measurements conducted over a range of U_∞ from 6 to 32 m s^{-1}, with an increment of 2 m s^{-1} in U_∞, corresponding to the *Re* range of (0.45–2.4) $\times 10^5$.

Figure 21 presents the variation of the captured five Strouhal numbers, St_r, St_s, St_w, St_g and St_l, with *Re*. The previously reported *St* for the Ahmed model of $\varphi = 25°$ is also included. Boucinha *et al.* (2011) detected from hot-wire measurements $St = 0.18$ above the rear window and $St = 0.36$ behind the base at $Re = 2.3 \times 10^5$. Minguez *et al.*'s (2008) data, i.e. $St = 0.27$ above the rear window and $St = 0.42$ behind the base, were obtained from numerical simulation at $Re = 8.9 \times 10^5$. Joseph *et al.* (2012) reported, based on hot-wire data, a significant rise in *St* from 0.33 to 0.50 over the rear window, but a slight increase from 0.51 to 0.53 behind the base, with *Re* increasing from 4.5×10^5 to 6.8×10^5. If their *St* measured above the rear window and behind the base are interpreted as St_r and St_w, respectively, we see a qualitative agreement between the data. For example, St_r rises with increasing *Re*. The deviation of these reports from each other and from ours is not unexpected in view of all the differences in techniques, experimental facilities, flow conditions, etc.

Both St_r and St_s display approximately linear rise with increasing *Re*. The data fit reasonably well to the equation $St = St' + mRe$, where constants St' and m, given in figure 21, are determined from the least-squares fitting to experimental data. The similar behaviour between St_r and St_s is internally consistent with the fact that their physical origins are the same, as found in § 4, both connected to vortices emanated

https://doi.org/10.1017/jfm.2015.332 Published online by Cambridge University Press

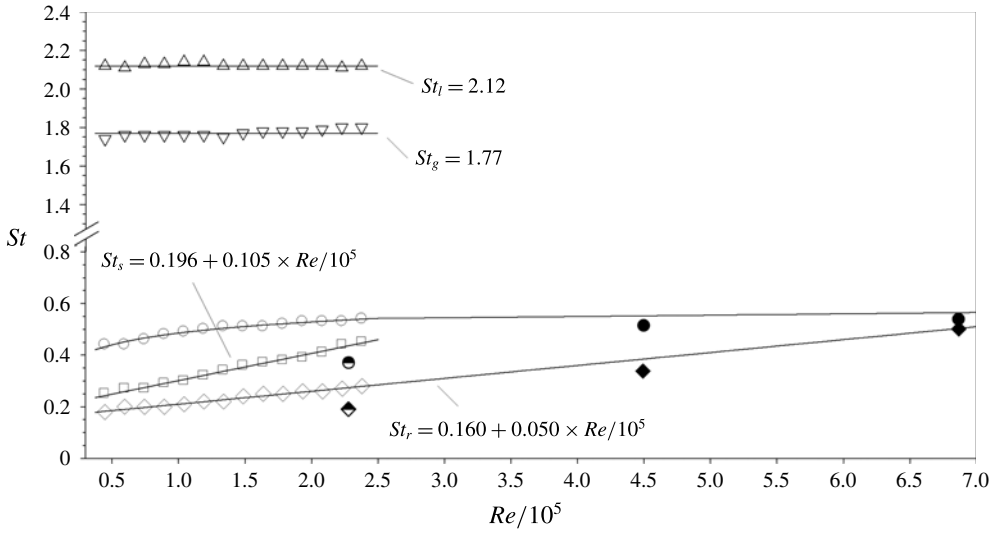


FIGURE 21. Dependence on Re of the Strouhal numbers: St_r (◇); St_s (□); St_w (○); St_g (▽); St_l (△). The three pairs of symbols ◆ and ●, and ⬘ and ◓, denote St_r and St_w, respectively, measured by Joseph *et al.* (2012) and Boucinha *et al.* (2011), respectively.

from the recirculation bubble formed near the leading edge of the roof or side surface. In flow around a rectangular flat plate, the frequency f of vortices emanated from the recirculation bubble was found to scale with U_∞/x_R (Kiya & Sasaki 1985; Tafti & Vanka 1991). It may be inferred that the frequency f_j ($j \in \{r \ or \ s\}$) of vortices emanated from the recirculation bubble near the leading edge of the roof or the side surface of the model is dictated by

$$f_j \sim U_\infty/x_{Rj}, \tag{5.1}$$

where x_{Rj} is the length of the bubble. Then, St_j may be rewritten as

$$St_j \sim (U_\infty/x_{Rj})\sqrt{A}/U_\infty = \sqrt{A}/x_{Rj} = 1/x^*_{Rj}, \quad j \in \{r \ or \ s\}. \tag{5.2}$$

Grandemange *et al.* (2013) studied the flow around an Ahmed body ($\varphi = 0°$) based on surface pressure measurements, and found that the recirculation bubbles (x^*_R) near the leading edge of the roof and side surface contracted in length from 0.4 to 0.04, with Re increasing from 1.1×10^5 to 2.9×10^6. Evidently, the rise in St_r and St_s for higher Re (figure 21) is attributed to a contraction in x^*_R. Based on flow visualization in a water tunnel, Spohn & Gillieron (2002) observed that the recirculation bubble formed near the leading edge of the roof was three-dimensional. The x_R value was largest in the symmetry plane ($y^* = 0$) and retreated towards the side surface, down to $x_R = 0$ at each end of the separation line. Note that the width of the roof ($W^* = 1.16$) is different from the height of the side surface ($H^* = 0.86$), which may cause a difference in size between the bubbles above the roof and on the lateral side and hence may be responsible for the different slopes in St_r and St_s versus Re.

The unsteady structures responsible for St_w arise from a mechanism very different from that for St_r and St_s, their generation being connected to the recirculation bubbles behind the vertical base (§ 3.3). As such, the dependence on Re of St_w is rather distinct from those of St_r and St_s and the nonlinearity is quite appreciable.

https://doi.org/10.1017/jfm.2015.332 Published online by Cambridge University Press

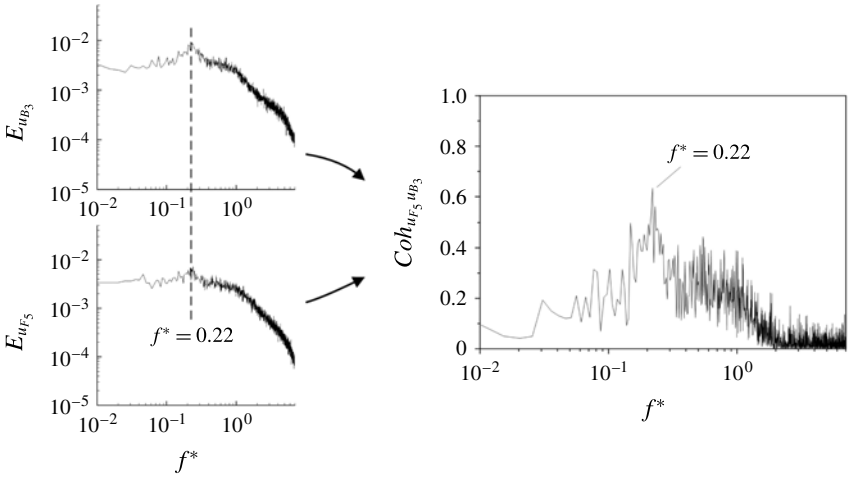


FIGURE 22. Spectral coherence between simultaneously measured hot-wire signals u_{F_5} and u_{B_3} at $Re = 1.2 \times 10^5$. Please refer to figures 3 and 17 for the locations of B_3 and F_5.

The values of St_l and St_g are 2.12 and 1.77, respectively, and vary little for the Re range examined (figure 21). As discussed earlier, the two frequencies are ascribed to vortices generated by the cylindrical struts located at $x^* = -2.52$ and $y^* = \pm 0.49$ and $x^* = -1.11$ and $y^* = \pm 0.49$, respectively. The results are internally consistent with the fact that the Strouhal number in the wake of a circular cylinder remains nearly constant, i.e. $St_D \approx 0.2$, for $Re_D = 3.0 \times 10^2$ to 1.0×10^5 (e.g. Schlichting & Gersten 2000). The value of St_g is lower than that of St_l by approximately 16 % since the fluid between the floor and the model underside is decelerated on moving downstream due to the boundary layers formed over both the floor and the model underside.

The predominant peak at St_a in E_u, such as the peak at $f^* = 0.14$ in figure 17, is not evident any more as Re exceeds 1.0×10^5 (not shown). At higher Re, the separation bubble near the leading edge of the roof (§ 4) is reduced in length (Grandemange *et al.* 2013), and its pulsation is thus attenuated. Naturally, the oscillation of the longitudinal vortex core may be impaired and may even vanish, accounting for the disappearance of St_a.

As illustrated in figure 22, at $Re = 1.2 \times 10^5$, both $E_{u_{B_3}}$ and $E_{u_{F_5}}$ display a predominant peak at the same frequency ($St_r = 0.22$), where hot-wire signals u_{F_5} and u_{B_3} are simultaneously measured at F_5 above the roof (figure 17) and B_3 (figure 3*b*) over the rear window. The $Coh_{u_{F_5}u_{B_3}}$ value shows a pronounced peak, reaching 0.62 at this frequency. The $Coh_{u_{E_4}u_{C_3}}$ between u_{E_4} and u_{C_3} (figure 23) simultaneously obtained at E_4 over the side surface (figure 19) and C_3 near the side edge of the rear window (figure 3*c*) at $Re = 1.2 \times 10^5$, respectively, displays a pronounced peak, with its magnitude reaching 0.92, at $St_s = 0.32$. Both $E_{u_{L_1}}$ and $E_{u_{L_4}}$ (figure 24) of u_{L_1} and u_{L_4} simultaneously measured at L_1 and L_4 in the symmetry plane behind the base (figure 7) exhibit a predominant peak at $St_w = 0.50$, which is ascribed to the organized structures emanated from the upper and lower recirculation bubbles behind the base. Similarly to the observation made at $Re = 0.62 \times 10^5$ (figure 9*a*), the spectral phase shift $\Phi_{u_{L_1}u_{L_4}}$ between u_{L_1} and u_{L_4} is near π at $St_w = 0.50$, indicating an antiphase relationship. By comparing the results at $Re = 1.2 \times 10^5$ with those at $Re = 0.62 \times 10^5$, it may be concluded that the Re effect on the connections between structures at different locations is insignificant.

https://doi.org/10.1017/jfm.2015.332 Published online by Cambridge University Press

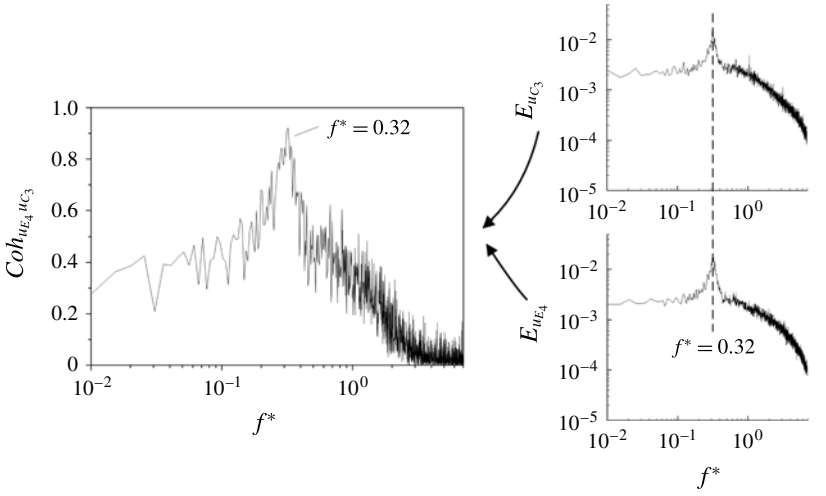


FIGURE 23. Spectral coherence between simultaneously measured hot-wire signals u_{E_4} and u_{C_3} at $Re = 1.2 \times 10^5$. Please refer to figures 3 and 19 for the locations of C_3 and E_4.

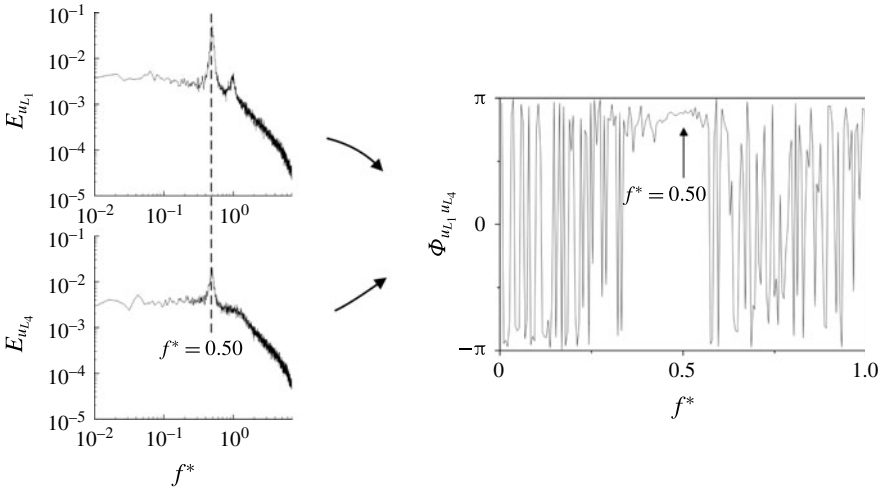


FIGURE 24. Spectral phase between hot-wire signals simultaneously measured at L_1 and L_4 at $Re = 1.2 \times 10^5$. Please refer to figure 7 for the locations of L_1 and L_4.

6. Turbulent intensity effect

The values of E_u (figure 25) measured at $T_u = 7.8\,\%$ for $Re = 0.62 \times 10^5$ exhibit a number of changes from their counterparts measured at $T_u = 0.3\,\%$ (figures 5*b*, 7, 15, 17*a* and 19). Firstly, there is no pronounced spectral peak in E_u measured at D_1–D_5 ($x^* = -2.33$, $z^* = 0.95$) near the leading edge of the roof (figure 25). In comparison, E_u measured at the same locations at $T_u = 0.3\,\%$ (figure 17*a*) displays two predominant frequencies, i.e. $St_r = 0.20$ at $y^* = 0$ and over $y^* = 0.29$–0.36, and $St_a = 0.14$ over $y^* = 0.14$–0.22, respectively. The former is attributed to the vortices emanated from the recirculation bubble near the leading edge of the roof, and the latter to the oscillation of the core of longitudinal vortices originated from bubble pulsation. The observation is fully consistent with previous reports in the literature.

https://doi.org/10.1017/jfm.2015.332 Published online by Cambridge University Press

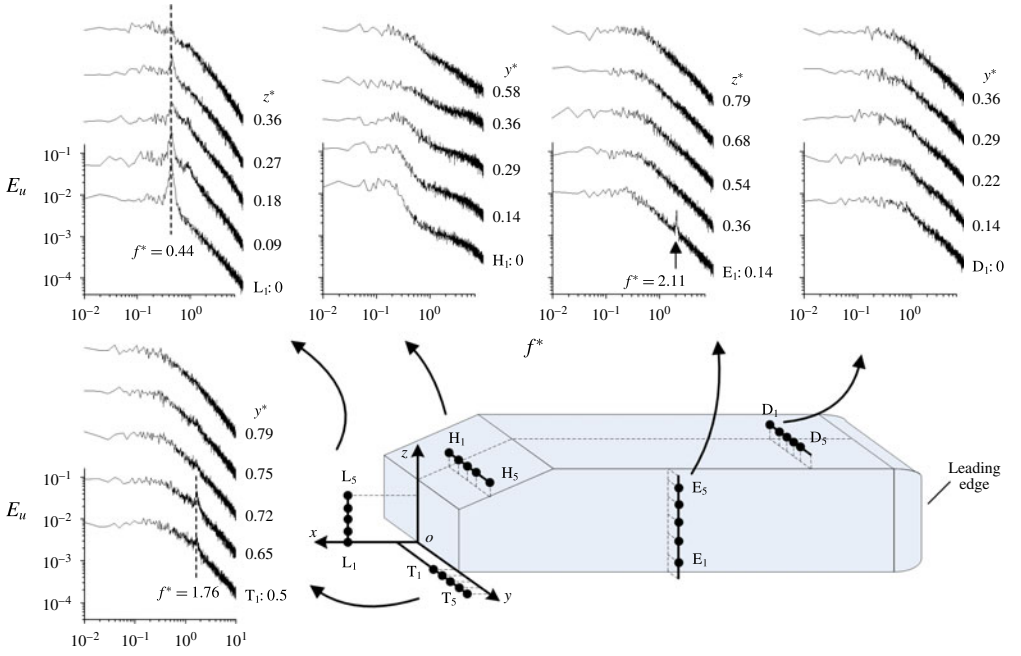


FIGURE 25. Power spectral density function E_u of the hot-wire signal measured around the model at $T_u = 7.8\,\%$. Please refer to figures 5, 7, 15, 17 and 19 for the locations of H_1–H_5, L_1–L_5, T_1–T_5, D_1–D_5 and E_1–E_5, respectively.

Conan, Anthoine & Planquart (2011) performed oil visualization measurements on the front of an Ahmed body at $Re = 8.9 \times 10^5$, and observed a flow separation region near the leading edge of the roof. They then deployed a strip of sandpaper before the separation line to force the transition to turbulence. As a result, flow separation was suppressed. Wang *et al.* (2014) studied the effect of T_u on the flow structures around an aerofoil at different angles (α) of attack. At $\alpha = 5°$–$12°$, they found that the increased T_u acted to promote the shear layer transition after flow separation near the leading edge, and the separation bubble was significantly suppressed. It may be concluded that the recirculation bubble near the leading edge of the roof must have been suppressed at $T_u = 7.8\,\%$. Consequently, E_u measured at D_1–D_5 exhibits no pronounced peaks. By the same token, the spectral peak at $St_s = 0.27$ observed for $T_u = 0.3\,\%$ in E_u (figure 19) vanishes at $T_u = 7.8\,\%$ (figure 25) since the recirculation bubble near the leading edge of the side face is also suppressed at the higher T_u.

Secondly, a rather broad hump occurs over $f^* = 0.1$–0.3 in E_u measured at H_1–H_5 ($x^* = -0.17$, $z^* = 0.79$) and $y^* = 0$–0.29 over the rear window at $T_u = 7.8\,\%$, in contrast to the less broad peak at $St_r = 0.20$ in E_u measured over $y^* = 0$–0.36 at $T_u = 0.3\,\%$ (figure 5), which is attributed to the spanwise vortices emanated from the separation bubble at the upper edge of the rear window. It was earlier found that this frequency is dictated by that of the vortices emanated from the separation bubble near the leading edge of the roof. It may be inferred that the spanwise vortices may form less periodically without the upstream vortex excitation at $T_u = 7.8\,\%$.

Thirdly, the quasi-periodic structures at $St_w = 0.44$ alternately emanated from the upper and lower recirculation bubbles behind the base at $T_u = 0.3\,\%$ (figure 7) remain at $T_u = 7.8\,\%$; a pronounced peak is evident at $f^* = St_w = 0.44$ in E_u (figure 25) measured along L_1–L_5 ($x^* = 0.4$, $y^* = 0$) behind the base.

https://doi.org/10.1017/jfm.2015.332 Published online by Cambridge University Press

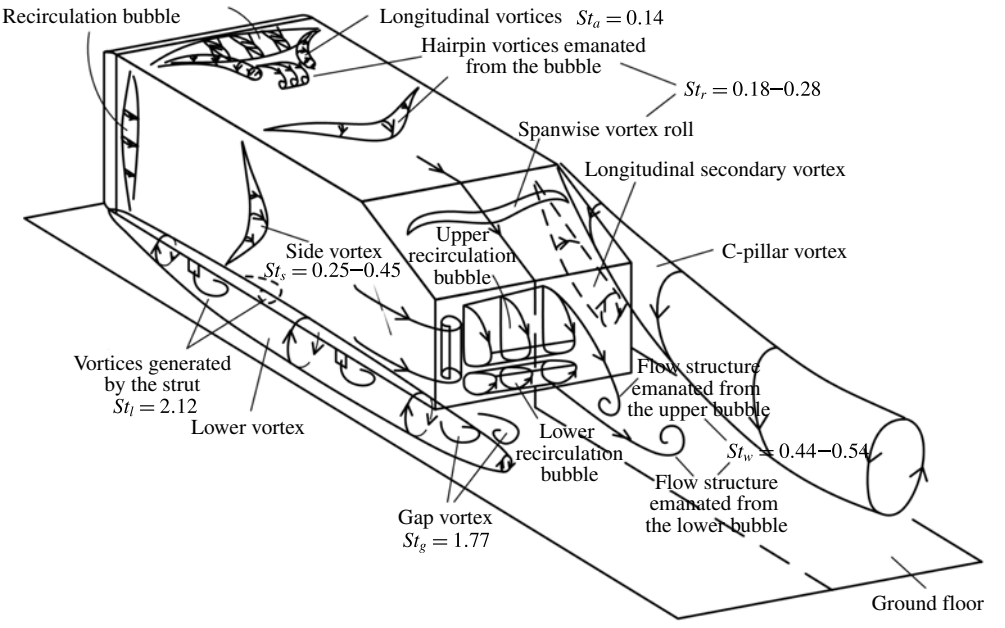


FIGURE 26. A conceptual model of the flow structure around the Ahmed model.

Finally, the flow structures associated with $St_l = 2.12$ and $St_g = 1.77$, detected at $T_u = 0.3\,\%$ near the lower edge of the side surface and behind the lower edge of the base, respectively (figures 15 and 19), are also identifiable at $T_u = 7.8\,\%$. As shown in figure 25, E_u measured along E_1–E_5 ($x^* = -1.27$, $y^* = 0.63$) near the side surface displays a predominant peak at $f^* = St_l = 2.11$ at $z^* = 0.14$ near the floor, and that along T_1–T_5 ($x^* = 0.09$, $z^* = 0$) behind the lower edge of the base shows a peak at $f^* = St_l = 1.76$ over $y^* = 0.5$–0.65. The slight deviation in St_l and St_g between the two cases is well within experimental uncertainties.

7. A conceptual model of the flow structure

A conceptual model is proposed for the flow structure of the high-drag regime around the Ahmed model ($\varphi = 25°$), as sketched in figure 26, based on the present data and those in the literature. This model covers the flow structure above the roof, over the side surface and the rear window, and behind the base, including all the indicative predominant frequencies of the unsteady structures.

The flow separates and then reattaches near the leading edge of the roof, producing a periodically pulsating recirculation bubble (Minguez *et al.* 2008). Two predominantly longitudinal counter-rotating vortices occur behind the bubble, whose origin is two foci at the ends of the flow separation line (Spohn & Gillieron 2002). The longitudinal vortex core oscillates at a frequency of $St_a = 0.14$ at $Re = 0.62 \times 10^5$ (figure 17*a*), resulting from the bubble pulsation. The frequency $St_r = 0.18$–0.28 in the Re range of $(0.45$–$2.4) \times 10^5$ (figures 17*a*,*b* and 21) is linked to three-dimensional hairpin vortices (Krajnović & Davidson 2005*a*; Franck *et al.* 2009), which emanate from the recirculation bubble and advect downstream along the roof. Behind the

https://doi.org/10.1017/jfm.2015.332 Published online by Cambridge University Press

recirculation bubble formed near the leading edge of the side surface, side vortices occur at a frequency $St_s = 0.25$–0.45 given $Re = (0.45$–$2.4) \times 10^5$ (figures 19 and 21).

The bubble pulsation and hairpin vortex emanation bear similarity to observations in flow around a blunt flat plate. The bubble in flow around a blunt flat plate is characterized by periodic enlargement and shrinkage, i.e. bubble pulsation, and the shear layer rolls up behind the bubble, forming vortices. Kiya & Sasaki (1985) captured experimentally two distinct frequencies, i.e. $0.12U_\infty/x_R$ and $0.65U_\infty/x_R$, which were ascribed to the recirculation bubble pulsation and vortex emanation from the bubble, respectively. Tafti & Vanka (1991) extracted numerically the recirculation bubble pulsation frequency at $0.15U_\infty/x_R$ and the vortex emanation frequency at $0.6U_\infty/x_R$. Spohn & Gillieron (2002) also reported experimentally the frequency of vortex emanation from the bubble, which exceeded 10 times the pulsation frequency of the recirculation bubble. Note that the bubble pulsation frequency reported by Kiya & Sasaki (1985) and Tafti & Vanka (1991) is of the order of one-quarter of the vortex emanation frequency, smaller than ours, which is approximately three-quarters. Such a discrepancy may be linked to a difference in the geometry of the leading edge of the model and the three-dimensionality, as discussed earlier, of the recirculation bubble between theirs and ours.

Photographs from flow visualization (figure 4) indicate that flow separates from the upper sharp edge of the rear window and then reattaches on the slant surface, forming a very small recirculation bubble. This bubble grows with increasing φ (Conan *et al.* 2011) and bursts when φ reaches 30° (Ahmed *et al.* 1984). The previously observed quasi-periodic spanwise vortices over the rear window (Wang *et al.* 2013) are found with a predominant frequency of $St_r = 0.18$–0.28 for the Re range of $(0.45$–$2.4) \times 10^5$, as determined from the hot-wire signal spectrum measured over $y^* = 0$–0.36 (figure 5). It is further found that the spanwise vortices are connected to the hairpin vortices formed behind the separation bubble near the leading edge of the roof. In fact, the two unsteady structures are highly correlated, with the predominant frequency of the former dictated by that of the latter (figure 18). This connection suggests that the shear layer formed above the roof has a significant impact on flow separation and vortex shedding from the slanted rear window. The shear layer rolls up about the side edge of the slant surface due to the pressure difference between the flow coming off the side surface and that over the rear window, thus forming the C-pillar vortices (Ahmed *et al.* 1984). On the other hand, the side vortices are formed at $St_s = 0.25$–0.45, for $Re = (0.45$–$2.4) \times 10^5$, over the side surface of the model. Under the rollup effect of the shear layer coming off the side surface along the side edge of the rear window, the side vortices are probably wrapped up around the slanted side edge. This may explain why St_s is detected where the C-pillar vortex occurs (figures 3*c*, 5 and 21).

One row of alternately signed streamwise structures occurs at the same level of the upper edge of the base. The C-pillar vortex induces the adjacent longitudinal vorticity concentration of opposite sign, which is considerably weaker. For the same reason, another vorticity concentration of even weaker strength can be induced next to this secondary vortex.

The shear layers roll up at the upper and lower edges of the vertical base, forming the upper and lower recirculation bubbles. The coherent structures are alternately emanated at $St_w = 0.44$–0.54 for $Re = (0.45$–$2.4) \times 10^5$ from the two bubbles in the central region of the wake (figures 8 and 21). The structure from the upper bubble appears sweeping towards the ground and then breaking up, whilst that from the lower bubble is emanated upwards. The latter is found to persist significantly longer than the former and grows downstream with spanwise extent increasing, as inferred

https://doi.org/10.1017/jfm.2015.332 Published online by Cambridge University Press

from the power spectral density function of the hot-wire signals (figure 7) and the spectral phase shift between the signals (figure 9). The C-pillar vortex and the upper recirculation bubble interact with each other and merge downstream, forming one pair of counter-rotating trailing vortices in the wake (figure 14). The previously observed lower vortex (Krajnović & Davidson 2005*a*), gap vortex and side vortex (Wang *et al.* 2013) are all incorporated in this model. The lower vortex is formed near the lower edge of the side surface due to the pressure difference between the flow inside and outside the gap between the model underside and the floor (e.g. Wang *et al.* 2013). The unsteady structures at $St_l \approx 2.12$ are detected near the lower edge of the side surface (figures 19 and 21), which are generated by the upstream struts located at $x^* = -2.52$ and $y^* = \pm 0.49$. On the other hand, the gap vortex is generated by the downstream struts located at $x^* = -1.11$ and $y^* = \pm 0.49$, and its predominant frequency is $St_g \approx 1.77$ (figures 15 and 21).

The flow structures shown in figure 26 are all obtained based on instantaneous data. It should be noted that some instantaneous flow structures, e.g. the pair of C-pillar vortices, and the upper and lower recirculation bubbles behind the base, remain after the time-averaging process, as is evident in the classical Ahmed time-averaged flow structure model (Ahmed *et al.* 1984), while others, e.g. the alternately emanated organized structures from the upper and lower recirculation bubbles behind the base and the spanwise vortex rolls over the slanted surface, may disappear due to a jitter or change in their spatial locations during the time-averaging process.

Instantaneous flow structures, including the vortices emanated from the recirculation bubbles formed near the leading edge of the roof and side surface, and the pair of longitudinal vortices originating from two foci at each end of the separation line near the leading edge of the roof, fail to be detected at $Re > 2.4 \times 10^5$. Based on the surface pressure measurements, Grandemange *et al.* (2013) found that the recirculation bubbles near the leading edge of the roof and side surface shrunk significantly in length with increasing Re. Apparently, the vanishing of these vortices is connected to the suppressed recirculation bubbles with increasing Re. This observation bears similarity to that made as T_u is increased at $Re = 0.62 \times 10^5$, where the two vortex frequencies, i.e. $St_r = 0.20$ and $St_s = 0.27$, captured at $T_u = 0.3\,\%$ over the roof and the side face, respectively, cannot be detected at $T_u = 7.8\,\%$ (figure 25). Wang *et al.* (2014) found that, at a low Reynolds number Re_c, based on the chord length of the aerofoil, the influence of T_u on the aerofoil wake exhibited similarity to that of Re_c. For example, both T_u and Re_c, if increased, could cause early transition in the shear layer and hence reattachment, forming a separation bubble. The concept of the effective Reynolds number was proposed, which treated T_u as an additional Re_c, with a caveat that the two effects are not identical in every aspect. It seems plausible based on the present observations that T_u may be treated as an additional Re in the Ahmed model wake, though more experimental data are required to document the similarity and differentiation between the two effects.

8. Conclusions

A rather exhaustive experimental investigation has been conducted on the quasi-periodic unsteady flow structures around an Ahmed model ($\varphi = 25^\circ$) and their predominant frequencies. Comprehensive measurements were performed for $Re = (0.45\text{–}2.4) \times 10^5$ above the roof, over the side face and the rear window, and behind the base. A total of six distinct predominant frequencies have been identified, with

https://doi.org/10.1017/jfm.2015.332 Published online by Cambridge University Press

St ranging from 0.14 to 2.12, each corresponding to distinct unsteady flow structures, as summarized below.

Two types of unsteady flow structures are found over the rear window. One is the spanwise vortex roll, characterized by a predominant frequency of $St_r = 0.18$–0.28. The other is detected near the side edge of the rear window, coinciding spatially with the C-pillar vortex, with a predominant frequency of $St_s = 0.25$–0.45.

One quasi-periodic structure is detected behind the base. Its predominant frequency is $St_w = 0.44$–0.54. This unsteady structure results from the alternate emanation of organized structures from the upper and lower recirculation bubbles behind the base, as supported by flow visualization and PIV data and a spectral phase shift of near π at St_w between simultaneously measured hot-wire signals in the upper and lower recirculation bubbles. The structure emanated from the upper recirculation bubble is found to be relatively short-lived, whilst the other from the lower recirculation bubble persists significantly farther downstream. A physical process is proposed for the pulsation of the upper and lower recirculation bubbles and the generation of the quasi-periodic structure, which is fully consistent with experimental observations.

Two different unsteady flow structures, with $St_l = 2.12$ and $St_g = 1.77$, respectively, are captured behind the vertical base and near the floor, which originate from vortex shedding from the upstream and downstream cylindrical struts, respectively. The latter coincides spatially with the previously observed gap vortex.

Two types of quasi-periodic unsteady flow structures are detected above the roof. One occurs at $St_a = 0.14$ at $Re = 0.62 \times 10^5$ near the leading edge of the roof, which is not evident any more as Re exceeds 1.0×10^5 and is ascribed to pulsation of the flow separation bubble. The other is observed behind the separation bubble, with a predominant frequency of $St_r = 0.18$–0.28. This structure is emanated from the bubble, like that found in a rectangular plate (Kiya & Sasaki 1985). The predominant frequency of this structure is identical to that ($St_r = 0.18$–0.28) of the spanwise vortex roll formed over the rear window. In fact, the two structures are strongly correlated, with $Coh_{u_{F_5} u_{B_3}}$ reaching 0.63 at $St_r = 0.20$ at $Re = 0.62 \times 10^5$. It may be inferred that the predominant frequency of the spanwise vortex rolls is actually dictated by that emanated from the separation bubble near the leading edge of the roof.

Side vortices are observed at $St_s = 0.25$–0.45 over the side surface. As for the case above the roof, the side vortex is emanated from the recirculation bubble formed near the leading edge of the side surface. The side vortex occurs at the same frequency as that measured near the side edge of the rear window. The two unsteady structures are excellently correlated, with $Coh_{u_{H_4} u_{C_3}}$ reaching 0.96 at St_s for $Re = 0.62 \times 10^5$. Evidently, the unsteady structures of St_s detected near the side edge of the rear window stem from the side vortices.

The Re effect on the Strouhal numbers, i.e. St_r, St_s, St_w, St_g and St_l, is also investigated. While St_g and St_l vary little with Re, St_r and St_s increase almost linearly and slowly with Re. However, the dependence of St_w on Re exhibits an appreciable nonlinearity. The Re effect is insignificant on the interrelationships between the structures.

The influence of T_u on the flow structures around the Ahmed model is examined at $Re = 0.62 \times 10^5$. As T_u is increased to 7.8 %, the unsteady structures of $St_r = 0.20$ and $St_s = 0.27$ above the roof and over the side surface, respectively, vanish, and the spanwise vortices over the rear window appear less periodically. On the other hand, the structures at $St_w = 0.44$, $St_l = 2.12$ and $St_g = 1.77$ do not exhibit strong dependence on T_u.

https://doi.org/10.1017/jfm.2015.332 Published online by Cambridge University Press

One conceptual flow structure model is proposed for the Ahmed model. This model incorporates all the coherent structures, found presently as well as previously, and the dimensionless frequencies identified for all the unsteady coherent structures, thus providing a rather comprehensive picture of the flow structure. The range of dimensionless frequencies (0.14–2.12) found for various unsteady structures also compromises the wide scattering of previously reported Strouhal numbers.

Acknowledgements

Y.Z. wishes to acknowledge support given to him from the Research Grants Council of HKSAR through grant GRF 531912 and from the Scientific Research Fund of Shenzhen Government through grants JCYJ20130329154125496 and JCYJ20120613144508935.

REFERENCES

AHMED, S. R., RAMM, G. & FALTIN, G. 1984 Some salient features of the time-averaged ground vehicle wake. *SAE Technical paper 840300*, 1–30, Society of Automotive Engineers, Inc., Warrendale, PA.

ALAM, M. M., ZHOU, Y. & WANG, X. W. 2011 The wake of two side-by-side square cylinders. *J. Fluid Mech.* **669**, 432–471.

ANGELIS, W., DRIKAKIS, D., DURST, F. & KHIER, W. 1996 Numerical and experimental study of the flow over a two-dimensional car model. *J. Wind Engng Ind. Aerodyn.* **62**, 57–79.

ANTONIA, R. A., ZHOU, Y. & MATSUMARA, M. 1993 Spectral characteristics of momentum and heat transfer in the turbulent wake of a circular cylinder. *Exp. Therm. Fluid Sci.* **6**, 371–375.

AUBRUN, S., MCNALLY, J., ALVI, F. & KOURTA, A. 2011 Separation flow control on a generic ground vehicle using steady microjet arrays. *Exp. Fluids* **51**, 1177–1187.

BEAUDOIN, J. F. & AIDER, J. L. 2008 Drag and lift reduction of a 3D bluff body using flaps. *Exp. Fluids* **44**, 491–501.

BOUCINHA, V., WEBER, R. & KOURTA, A. 2011 Drag reduction of a 3D bluff body using plasma actuators. *Intl J. Aerodyn.* **1**, 262–280.

BRUNEAU, C., CREUSE, E., DELPHINE, D., GILLIERON, P. & MORTAZAVI, I. 2011 Active procedures to control the flow past the Ahmed body with a 25° rear window. *Intl J. Aerodyn.* **1**, 299–317.

BRUNN, A., WASSEN, E., SPERBER, D., NITSCHE, W. & THIELE, F. 2007 Active drag control for a generic car model. In *Active Flow Control*, NNFM, vol. 95, pp. 247–259. Springer.

CONAN, B., ANTHOINE, J. & PLANQUART, P. 2011 Experimental aerodynamics study of a car-type bluff body. *Exp. Fluids* **50**, 1273–1284.

FRANCK, G., NIGRO, N., STORTI, M. & D'ELIA, J. 2009 Numerical simulation of the flow around the Ahmed vehicle model. *Latin Am. Appl. Res.* **39**, 295–306.

GRANDEMANGE, M., GOHLKE, M. & CADOT, O. 2013 Turbulent wake past a three-dimensional blunt body. Part 1. Global modes and bi-stability. *J. Fluid Mech.* **722**, 51–84.

HEFT, A. I., INDINGER, T. & ADAMS, N. A. 2011 Investigations of unsteady flow structures in the wake of a realistic generic car model. *AIAA Paper* 2011-3669.

HUANG, J. F., ZHOU, Y. & ZHOU, T. M. 2006 Three-dimensional wake structure measurement using a modified PIV technique. *Exp. Fluids* **40**, 884–896.

HUCHO, W. H. & SOVRAN, G. 1993 Aerodynamics of road vehicles. *Annu. Rev. Fluid Mech.* **25**, 485–537.

JOSEPH, P., AMANDOLESE, X. & AIDER, J. L. 2012 Drag reduction on the 25° slant angle Ahmed reference body using pulsed jets. *Exp. Fluids* **52**, 1169–1185.

KAISER, E., NOACK, B. R., CORDIER, L., SPOHN, A., SEGOND, M., ABEL, M., DAVILLER, G., ÖSTH, J., KRAJNOVIĆ, S. & NIVEN, R. K. 2014 Cluster-based reduced-order modelling of a mixing layer. *J. Fluid Mech.* **754**, 365–414.

https://doi.org/10.1017/jfm.2015.332 Published online by Cambridge University Press

KIYA, M. & SASAKI, K. 1985 Structure of large-scale vortices and unsteady reverse flow in the reattaching zone of a turbulent separation bubble. *J. Fluid Mech.* **154**, 463–491.

KOURTA, A. & LECLERC, C. 2013 Characterization of synthetic jet actuation with application to Ahmed body wake. *Sensors Actuators* A **192**, 13–26.

KRAJNOVIĆ, S. 2014 Large eddy simulation exploration of passive flow control around an Ahmed body. *Trans. ASME: J. Fluids Engng* **136**, 121103.

KRAJNOVIĆ, S. & DAVIDSON, L. 2005*a* Flow around a simplified car. Part 2: understanding the flow. *Trans. ASME: J. Fluids Engng* **127**, 919–928.

KRAJNOVIĆ, S. & DAVIDSON, L. 2005*b* Influence of floor motions in wind tunnels on the aerodynamics of road vehicles. *J. Wind Engng* **93**, 677–696.

KRENTEL, D., MUMINOVIC, R., BRUNN, A., NITSCHE, W. & KING, R. 2010 Application of active flow control on generic 3D car models. In *Active Flow Control*, NNFM, vol. 108, pp. 223–239. Springer.

LIENHART, H. & BECKER, S. 2003 Flow and turbulence structures in the wake of a simplified car model. *SAE Technical Paper* 2003-01-0656, Society of Automotive Engineers, Inc., Warrendale, PA.

LOGDBERG, O., FRANSSON, J. H. M. & ALFREDSSON, P. H. 2009 Streamwise evolution of longitudinal vortices in a turbulent boundary layer. *J. Fluid Mech.* **623**, 27–58.

MINGUEZ, M., PASQUETTI, R. & SERRE, E. 2008 High-order large-eddy simulation of flow over the Ahmed body car model. *Phys. Fluids* **20**, 095101.

ÖSTH, J., NOACK, B. R., KRAJNOVIĆ, S., BARROS, D. & BORÉE, J. 2014 On the need for a nonlinear subscale turbulence term in POD models as exemplified for a high-Reynolds-number flow over an Ahmed body. *J. Fluid Mech.* **747**, 518–544.

SCHLICHTING, H. & GERSTEN, K. 2000 *Boundary Layer Theory*, 8th revised. p. 22. Springer.

SHABAKA, I. M. M. A., MEHTA, R. D. & BRADSHAW, P. 1985 Longitudinal vortices imbedded in turbulent boundary layers. Part 1. Single vortex. *J. Fluid Mech.* **155**, 37–57.

SPOHN, A. & GILLIERON, P. 2002 Flow separations generated by a simplified geometry of an automotive vehicle. In *IUTAM Symposium: Unsteady Separated Flows*. Kluwer Academic.

TAFTI, D. K. & VANKA, S. P. 1991 A three-dimensional numerical study of flow separation and reattachment on a blunt plate. *Phys. Fluids* A **3**, 2887–2909.

THACKER, A., AUBRUN, S., LEROY, A. & DEVINANT, P. 2010 Unsteady analyses of the flow separation on the rear window of a simplified ground vehicle model. *AIAA Paper* 2010-4569.

THACKER, A., AUBRUN, S., LEROY, A. & DEVINANT, P. 2013 Experimental characterization of flow unsteadiness in the centerline plane of an Ahmed body rear slant. *Exp. Fluids* **54**, 1479,1–16.

VINO, G., WATKINS, S., MOUSLEY, P., WATMUFF, J. & PRASAD, S. 2005 Flow structures in the near-wake of the Ahmed model. *J. Fluids Struct.* **20**, 673–695.

WANG, S., ZHOU, Y., ALAM, M. M. & YANG, H. 2014 Turbulent intensity and Reynolds number effects on an airfoil at low Reynolds numbers. *Phys. Fluids* **26**, 115107.

WANG, H. F., ZHOU, Y. & MI, J. 2012 Effects of aspect ratio on the drag of a wall-mounted finite-length cylinder wake in subcritical and critical regimes. *Exp. Fluids* **53**, 423–436.

WANG, X. W., ZHOU, Y., PIN, Y. F. & CHAN, T. L. 2013 Turbulent near wake of an Ahmed vehicle model. *Exp. Fluids* **54**, 1490,1–19.

WASSEN, E. & THIELE, F. 2008 Drag reduction for a generic car model using steady blowing. *AIAA Paper* 2008-3771.

WASSEN, E. & THIELE, F. 2010 Simulation of active separation control on a generic vehicle. *AIAA Paper* 2010-4702.

ZHANG, B. F., TO, S. & ZHOU, Y. 2013 Strouhal numbers of unsteady flow structures around a simplified car model. In *Fluid-Structure-Sound Interactions and Control, Proceedings of the 2nd Symposium on Fluid-Structure-Sound Interactions and Control* (ed. Y. Zhou, Y. Liu, L. Huang & D. Hodges), pp. 179–184. Springer.

ZHOU, Y. & ANTONIA, R. 1994 Critical points in a turbulent near-wake. *J. Fluid Mech.* **275**, 59–81.

ZHOU, Y., DU, C., MI, J. & WANG, X. W. 2012 Turbulent round jet control using two steady mini-jets. *AIAA J.* **50**, 736–740.

https://doi.org/10.1017/jfm.2015.332 Published online by Cambridge University Press